Draft version October 22, 2003
Preprint typeset using LaTeX style emulateapj v. 7/15/03

SUPERNOVA SIMULATIONS WITH BOLTZMANN NEUTRINO TRANSPORT: A COMPARISON OF METHODS

M. Liebendörfer[1,2,3], M. Rampp[4], H.-Th. Janka[4], A. Mezzacappa[2]

Draft version October 22, 2003

ABSTRACT

Accurate neutrino transport has been built into spherically symmetric simulations of stellar core collapse and postbounce evolution. The results of such simulations agree that spherically symmetric models with standard microphysical input fail to explode by the delayed, neutrino-driven mechanism. Independent groups implemented fundamentally different numerical methods to tackle the Boltzmann neutrino transport equation. Here we present a direct and detailed comparison of such neutrino radiation-hydrodynamical simulations for two codes, AGILE-BOLTZTRAN of the Oak Ridge-Basel group and VERTEX of the Garching group. The former solves the Boltzmann equation directly by an implicit, general relativistic discrete angle method on the adaptive grid of a hydrodynamics code with conservative first-order finite differencing. In contrast, the latter couples a variable Eddington factor technique with an explicit, moving-grid, conservative high-order Riemann solver with important relativistic effects treated by an effective gravitational potential. The presented study is meant to test both neutrino radiation-hydrodynamics implementations and to provide a data basis for comparisons and verifications of supernova codes to be developed in the future. The results are investigated in simulations of the core collapse and post-bounce evolution of a 13 $M_\odot$ star with Newtonian gravity and a 15 $M_\odot$ star with relativistic gravity.

Subject headings: supernovae: general—neutrinos—radiative transfer—hydrodynamics—relativity—methods: numerical

1. INTRODUCTION

Computer simulations are becoming more and more popular. They allow investigations of physics on office desks rather than explorations through hands-on experiments (This does not imply a transition from hard work to gaming). In the industrial context, the two approaches are not separable: the computer codes have to be validated. After a computer design has been completed, its relation to reality will inevitably be assessed in the manufacture and evaluation of prototypes. How about the growing importance of computer simulations in astrophysics - where are the measurements found to test aspects of a complex computer code in idealized setups, and where are the prototypes that validate the quality of the results in the targeted application? The first step of code development is accompanied by the verification of partial aspects of the code in simplified test problems where the solution is analytically known. The code can be improved step by step. Additionally, laboratory experiments may be used to further verify the code with accurate measurements in idealized setups. The transition to code validation is made when its capability to handle complicated coupled processes is tested and the completeness of the physical description is evaluated. In the industrial context, this is achieved by more comprehensive experiments and measurements, or, ultimately, by the comparison of computer designs with the properties of manufactured prototypes. We would now be tempted to relate the validation of computer generated results with real life prototypes in manufacturing to the comparison of astrophysical simulations with astronomical observations. This would, however, circumvent the goal of astrophysical simulations: One does not assume unknown physics in industrial design. Perfect agreement between a computer simulation and the behavior of a prototype can indeed be seen as proof of the quality of the computer code. The situation is different in astrophysics, where the understanding of the physics of an event is rather the goal than the ingredient. The comparison between simulation and observation is essential to demonstrate the physical understanding of the event, it cannot at the same time be used to qualify code performance. The gap in code validation between detached analytical test calculations and the astrophysical application can be bridged by code comparisons (Calder et al. 2002), based on the assumption that different numerical approaches are likely to show different strengths and weaknesses in simulations of complex physical systems. Differences in the simulation results are an indicator for uncertainties in the numerical methods.

In the present paper we document the detailed comparison of results from different supernova codes. Both of our codes aim to provide a solution to the Boltzmann neutrino transport equation in spherical symmetry. This is achieved by fundamentally different numerical methods: The code of the Oak Ridge-Basel group (AGILE-BOLTZTRAN) consists of a general relativistic time-implicit discrete-angle (S_N) Boltzmann solver, which is coupled in an operator split fashion to a general relativistic time-implicit hydrodynamics solver with a dynamical adaptive grid. It implements a direct finite difference representation of the Boltzmann equation (Mezzacappa & Bruenn 1993a; Mezzacappa &

[1] CITA, University of Toronto, Toronto, Ontario M5S 3H8, Canada
[2] Physics Division, Oak Ridge National Laboratory, Oak Ridge, Tennessee 37831-6354
[3] Department of Physics and Astronomy, University of Tennessee, Knoxville, Tennessee 37996-1200
[4] Max-Planck-Institut für Astrophysik, Karl-Schwarzschild-Strasse 1, D-85741 Garching, Germany

Messer 1999; Liebendörfer, Rosswog, & Thielemann 2002; Liebendörfer et al. 2004). The Garching code, VERTEX, is a one-dimensional version of a program that was developed to perform multi-dimensional supernova simulations with accurate ray-by-ray neutrino transport. It is based on the explicit, moving-grid, finite-volume hydrodynamics code PROMETHEUS, which employs a Riemann solver for constructing the solution of the hydrodynamics equations. The neutrino transport is handled in an operator-split step and is calculated by a variable Eddington factor closure of neutrino energy, number, and momentum equations, where the variable Eddington factor is derived from the formal solution of a spherically averaged model Boltzmann equation (Rampp & Janka 2002). In spherical symmetry, there is only one "ray" for the solution of the moments equations and the spherical averaging in the model Boltzmann equation is obsolete. Therefore, a convergence in the iterations between the moments equations and the closure from the model Boltzmann equation provides in spherical symmetry a solution of the complete Boltzmann equation.

This work has two main goals. (i) The direct comparison of two codes applied to the same challenging astrophysical scenario with concerted physics (spherical symmetry, progenitor models, nuclear and weak interaction physics, general relativistic effects). (ii) The production of reference results to test future supernova codes in the spherical limit. Electronic data files can be obtained from the authors.

Neutrinos play a crucial role in collapsing cores of massive stars. The loss of electron lepton number by the production and escape of electron neutrinos determines the collapse dynamics and the position where the supernova shock forms. Energy and lepton number transport by neutrino diffusion also govern the evolution of the nascent neutron star. The energy transfer by neutrinos to the medium that surrounds the protoneutron star may revive the stalled shock and thus drive a delayed explosion (Wilson 1985; Bethe & Wilson 1985). Neutrino interactions moreover set the proton-to-nucleon ratio and therefore the conditions for nucleosynthesis in the innermost supernova ejecta. Sustained energy deposition near the protoneutron star surface causes a post-explosion outflow of baryonic matter, the so-called neutrino-driven wind, which is discussed as a potential site for the formation of r-process elements (Woosley et al. 1994; Takahashi, Witti, & Janka 1994; Sumiyoshi et al. 2000; Wanajo et al. 2001; Thompson, Burrows, & Meyer 2001).

Deep inside the protoneutron star the absorption and scattering mean free paths of neutrinos are very small and therefore neutrinos diffuse and are in chemical equilibrium with the stellar plasma. With decreasing density the neutrino interaction lengths become larger, before, finally the neutrinos can stream freely. Since the reaction cross sections rise steeply with the neutrino energy, low-energy neutrinos decouple from the stellar background at higher densities. Most electron flavor neutrinos emerge from the accreting material at the base of the cooling region under semi-transparent conditions and propagate to the heating region where their angular distribution influences the energy deposition behind the shock. Neither diffusion nor free streaming is a good approximation in this important region where neutrinos strongly couple the dynamics of different layers on a short propagation time scale.

An accurate treatment of the neutrino transport and of neutrino-matter interactions therefore requires that we merge the information about the location of neutrino sources with neutrino opacities in the energy- and angle-dependent Boltzmann transport equation. The solution of the Boltzmann equation is also desirable to test approximations, the most elaborate of which are certainly multi-group flux-limited diffusion (Bruenn 1985; Myra et al 1987; Bruenn, DeNisco, & Mezzacappa 2001) and two-moment closure schemes (Bludman & Cernohorsky 1995; Smit, Cernohorsky, & Dullemond 1997). With the growing computer capability it has become feasible to provide solutions to the Boltzmann transport equation not only for the collapse phase (Mezzacappa & Bruenn 1993a), but also in consistent dynamical simulations of the post-bounce evolution (Rampp & Janka 2000; Mezzacappa et al. 2001; Liebendörfer et al. 2001; Thompson, Burrows, & Pinto 2003).

The paper is organized as follows. We will describe in Sect. 2 the stellar models and the physical ingredients that constitute the problem to be solved by our numerical methods. In Sect. 3 we will briefly resume characteristic features and capabilities of both neutrino radiation-hydrodynamics codes. In Sect. 4 our results for the two considered stellar models will be discussed with special focus on the differences between the runs. In Sect. 5 we shall summarize our findings and draw conclusions.

2. DESCRIPTION OF THE MODEL

2.1. *Progenitors*

We present in this paper two different models. One of them includes only the most essential physical ingredients; e.g., the transport of electron flavor neutrinos but not heavy-lepton neutrinos. It is meant to serve as a guideline for future code development and transport approximations. The model is based on a 13 $M_\odot$ progenitor of Nomoto & Hashimoto (1988). The 13 $M_\odot$ progenitor model has a tradition in supernova simulations, its exceptionally small iron core sustained the hope to produce prompt explosions. We call this run N13, as it is based on Newtonian gravity. A second run was launched from a 15 $M_\odot$ progenitor of Woosley & Weaver (1995). This progenitor has been widely used in supernova investigations, as it provides a model of a massive star in the middle of the mass range that is expected to end its life in a supernova. The run takes into account all neutrino flavors with "standard" input physics as listed in (Bruenn 1985) (some additional extensions are made in VERTEX). General relativistic effects are included in this physically more complete run, G15.

2.2. *Radiation Hydrodynamics in Spherical Symmetry*

The stellar progenitor model is evolved in time by means of the hydrodynamics and neutrino transport equations. Since there is no danger of grid entangling in spherical symmetry, we make use of the freedom in AGILE-BOLTZTRAN

to choose orthogonal comoving space-time coordinates and describe the interactions in the collision term in the most convenient comoving frame for the neutrino four-momentum (see e.g. (Cardall & Mezzacappa 2003) for a generalized discussion of coordinate choices for the radiation transport). In the metric of Misner & Sharp (1964); May & White (1966),

$$ds^2 = -\alpha^2 (cdt)^2 + \left(\frac{1}{\Gamma}\frac{\partial r}{\partial a}\right)^2 da^2 + r^2 \left(d\vartheta^2 + \sin^2\vartheta d\varphi^2\right), \tag{1}$$

the equations of radiation hydrodynamics in spherical symmetry can be written in the form (Lindquist 1966; Liebendörfer, Mezzacappa, & Thielemann 2001)

$$\frac{\partial}{\partial t}\left[\frac{\Gamma}{\rho}\right] = \frac{\partial}{\partial a}\left[4\pi r^2 \alpha u\right] \tag{2}$$

$$\frac{\partial}{\partial t}\left[\Gamma\left(1+\frac{e+J}{c^2}\right)+\frac{uH}{c^4}\right] = -\frac{\partial}{c^2\partial a}\left[4\pi r^2\alpha\left(up+u\rho K+\Gamma\rho H\right)\right] \tag{3}$$

$$\begin{aligned}\frac{\partial}{\partial t}\left[u\left(1+\frac{e+J}{c^2}\right)+\frac{\Gamma H}{c^2}\right] =& -\frac{\partial}{\partial a}\left[4\pi r^2\alpha\left(\Gamma p+\Gamma\rho K+\frac{u\rho H}{c^2}\right)\right] \\ & -\frac{\alpha}{r}\left[\left(1+\frac{e+3p/\rho+J+3K}{c^2}\right)\frac{Gm}{r}\right. \\ & -\left(1-\frac{2Gm}{rc^2}\right)(J-3K)-2\left(\frac{p}{\rho}+K\right) \\ & \left.+8\pi r^2\frac{G}{c^2}\left(\left(1+\frac{e+J}{c^2}\right)(p+\rho K)-\frac{\rho H^2}{c^4}\right)\right]\end{aligned} \tag{4}$$

$$\frac{\partial}{\partial a}\left[\frac{4\pi}{3}r^3\right] = \frac{\Gamma}{\rho} \tag{5}$$

$$\frac{\partial m}{\partial a} = \Gamma\left(1+\frac{e+J}{c^2}\right)+\frac{uH}{c^4} \tag{6}$$

$$\begin{aligned}\frac{\partial}{\partial t}\left[\frac{1}{4\pi r^2\rho}\frac{H}{c^4}\right] =& -\left(1+\frac{e+J}{c^2}\right)\frac{\partial\alpha}{\partial a}-\frac{1}{\rho c^2}\frac{\partial}{\partial a}\left[\alpha\left(p+\rho K\right)\right] \\ & +\frac{\alpha\Gamma}{4\pi r^3\rho c^2}\left(J-3K\right).\end{aligned} \tag{7}$$

The metric is based on an enclosed baryon mass label, a, and a coordinate time, t. It refers to the areal radius, r, the "Lorentz" factor, $\Gamma = \sqrt{1+(u/c)^2-2Gm/(rc^2)}$, and the lapse function, α. The angles ϑ and φ describe a two-sphere. The quantity $u = \alpha^{-1}\partial r/\partial t$ takes the place of a fluid velocity and m is the enclosed gravitational mass, proportional to the enclosed total energy. Both of our codes split these equations into hydrodynamics equations and transport equations. VERTEX employs Eulerian coordinates which can be obtained by a coordinate transformation. The fluid is specified in its rest frame by the rest mass density, ρ, specific internal energy, e, and electron number fraction, Y_e, for which an additional evolution equation (lepton number conservation) is solved. The hydrodynamics equations are closed by the equation of state, which gives the pressure, p, as a function of density, internal energy, and electron number. The zeroth, J, first, H/c, and second, K, angular moment of the monochromatic neutrino intensity (normalized by the rest-mass density) are determined by the transport equation which includes the interactions listed in Table (1) in the collision integral. Eq. (7) determines the lapse function. Eq. (6) allows us to integrate outwards from $a = 0$ to obtain the total energy; it translates to the Poisson equation in the Newtonian limit. Eq. (5) defines the general relativistic analogue to the Newtonian volume. Eq. (4) describes the change of radial momentum; to leading order it is proportional to $-Gm/(cr)^2 + (J-3K)/r$. Eq. (3) describes the evolution of the total energy. Note that there are no contributions from terms of zeroth and first order in c. Eq. (2) relates the evolution of the specific volume to the divergence of the velocity field.

2.3. *Nuclear and Weak Interaction Physics Input*

The equation of state describes the thermodynamic state of a fluid element based on density, ρ, temperature, T, and the composition. The relation between the specific internal energy and the pressure closes the system of hydrodynamics equations. For this comparison we use the equation of state of Lattimer & Swesty (1991). It assumes nuclear statistical equilibrium and is based on a liquid drop model for a representative nucleus with atomic number A and charge Z, surrounded by free alpha particles, protons, and neutrons. These baryons are immersed in an electron and positron gas that equilibrates with a photon gas by the pair creation process. The incompressibility modulus can be adjusted. We use a value of $K = 180$ MeV. Above nuclear density, where no isolated individual nuclei are present, the transition to a proton-neutron-electron gas is made by a Maxwell phase transition. In any of these cases, the composition at given temperature and density is determined by the specification of the electron fraction Y_e. At low densities/temperatures

TABLE 1
OVERVIEW OF ALL NEUTRINO-MATTER INTERACTIONS CONSIDERED IN THE N13 RUNS.

Reaction			Reference[a]
$\nu e^{\pm}$	$\rightleftharpoons$	$\nu e^{\pm}$	Mezzacappa & Bruenn (1993c); Cernohorsky (1994)
νA	$\rightleftharpoons$	νA	Bruenn (1985) (no ion-ion correlations!)
νN	$\rightleftharpoons$	νN	Bruenn (1985); Mezzacappa & Bruenn (1993c)
ν_en	$\rightleftharpoons$	e^-p	Bruenn (1985); Mezzacappa & Bruenn (1993c)
$\bar{\nu}_e$p	$\rightleftharpoons$	e^+n	Bruenn (1985); Mezzacappa & Bruenn (1993c)
$\nu_e A'$	$\rightleftharpoons$	$e^- A$	Bruenn (1985); Mezzacappa & Bruenn (1993c)
$\nu\bar{\nu}$	$\rightleftharpoons$	$e^- e^+$	Bruenn (1985)

[a]The references point to papers where information can be found about the approximations employed in the rate calculations. Details about the numerical implementation can be found in the methodical papers of (Rampp & Janka 2002) and (Mezzacappa & Messer 1999; Liebendörfer et al. 2004), respectively. In the first column the symbol ν represents any of the neutrinos ν_e, $\bar{\nu}_e$, the symbols e^-, e^+, n, p and A denote electrons, positrons, free neutrons and protons, and heavy nuclei, respectively, the symbol N means n or p.

the VERTEX code switches to an equation of state that considers electrons, positrons, photons, nucleons and nuclei consistent with the composition used in the progenitor model (Rampp & Janka 2002). The switch is triggered in N13 and G15 by a density threshold of $\rho < 6 \times 10^7$ g/cm^3. AGILE-BOLTZTRAN applies the same switch in the run N13, but considers in the low density domain only one nucleus, ^{28}Si. In run G15, silicon is converted to NSE under energy conservation at a burning temperature of 0.44 MeV (Mezzacappa et al. 2001).

As for the neutrino-matter interactions, we have chosen to use the conventional ("standard") opacities, i.e., a description which follows closely the one detailed by Bruenn (1985); Mezzacappa & Bruenn (1993c). Note, however, there are differences in the neutrino description employed by the Garching group. While AGILE-BOLTZTRAN treats the μ/τ neutrinos and antineutrinos separately, they are combined to one species in VERTEX. In order to save computer time, usually only electron neutrinos are considered in the VERTEX calculations during the core collapse phase. Tests have shown that taking into account also electron antineutrinos and the heavy-lepton neutrinos leads to only minuscule differences in this phase of the supernova evolution (their inclusion in the postbounce phase, however, is important as the comparison between the models N13 and G15 demonstrates in section 4). The Garching group routinely includes nucleon-nucleon bremsstrahlung as a source (or sink) for neutrino-antineutrino pairs. The reduction of coherent neutrino scattering off heavy ions due to ion-ion correlations and electron screening (Horowitz 1997) is also taken into account. These improvements were not included in AGILE-BOLTZTRAN because they have not been considered to be of primary importance (Bruenn & Mezzacappa 1997; Messer et al. 2003). Each group adhered to its "standard" in the physically more complete G15 run, while the Garching group switched off ion-ion correlations and nucleon-nucleon bremsstrahlung in the N13 run to assist an accurate comparison of the transport method.

3. NUMERICAL METHODS

The two codes follow very different approaches to evaluate the radiation moments J, H, and K. Contrary to flux-limiting and "gray" transport methods, neither of our methods needs to make assumptions about the angular or the spectral distribution of the radiation field. Important features and implementation details of the two codes are summarized in the following subsections.

3.1. AGILE-BOLTZTRAN

The concept and first implementation of BOLTZTRAN has been developed in (Mezzacappa & Bruenn 1993a,b,c) for core collapse simulations in the order v/c approximation. Essential for the computational efficiency of the implicit scheme is the storage of the interactions in a dynamical table which delivers consistent derivatives of all cross sections and thermodynamical quantities for the Newton-Raphson iterations in the solution of the nonlinear equations (Mezzacappa & Messer 1999; Messer 2000). For the highly dynamical situation after bounce, BOLTZTRAN has been coupled to the hydrodynamics code AGILE. The finite differencing has been refined and extended to solve the general relativistic Eqs. (2-8) (Liebendörfer 2000; Liebendörfer, Rosswog, & Thielemann 2002; Liebendörfer et al. 2004).

3.1.1. *Hydrodynamics*

The hydrodynamics part of the Lagrangian Eqs. (2-7) is solved by implicit conservative finite differencing. One strength is the implementation of a dynamically moving adaptive grid following Winkler, Norman, & Mihalas (1984) and Dorfi & Drury (1987). In the general relativistic extension, it is equivalent to a resolution-dependent choice of shift vectors, that allow a continuous coordinate translation in the radial direction during the evolution of the model. Artificial viscosity has been included in a consistent, but causality violating, manner based on the tensor viscosity of Tscharnuter & Winkler (1979). It provides the mechanism for energy dissipation in the shock front and defines the shock width such that the number of attracted adaptive grid points does not grow beyond limits. A major advantage of the adaptive grid is the dynamical allocation of computational zones to regions where they are needed. The zoning for hydrodynamics and neutrino transport is always kept congruent for consistency reasons. During the evolution of the model, one group of grid points follows the shock, while another resolves the steep density gradient between the

outer layers of the protoneutron star and the infalling matter, where most of the electron flavor neutrinos stream away. The use of artificial viscosity is not a disadvantage of the method, as it only plays a minor local role in stabilizing the shock front (typically $\sim$ 10 zones are distributed across a few percent of the shock radius). A disadvantage of the adaptive grid approach in its current implementation is the numerical diffusion introduced by the first-order advection prescription in regions where the adaptive grid does not concentrate its zones, e.g. in a rarefaction wave or at sharp discontinuities of the composition. The implementation of AGILE has been described and tested in detail in (Liebendörfer, Rosswog, & Thielemann 2002).

3.1.2. *Neutrino Transport*

The neutrino transport part, BOLTZTRAN, solves the Boltzmann transport equation,

$$\begin{aligned} C = & \frac{\partial F}{\alpha \partial t} + \frac{\mu}{\alpha}\frac{\partial}{\partial a}\left[4\pi r^2 \alpha \rho F\right] \\ & + \Gamma\left(\frac{1}{r} - \frac{1}{\alpha}\frac{\partial \alpha}{\partial r}\right)\frac{\partial}{\partial \mu}\left[\left(1-\mu^2\right)F\right] + \left(\frac{\partial \ln \rho}{\alpha \partial t} + \frac{3u}{r}\right)\frac{\partial}{\partial \mu}\left[\mu\left(1-\mu^2\right)F\right] \\ & - \mu\Gamma\frac{1}{\alpha}\frac{\partial \alpha}{\partial r}\frac{1}{E^2}\frac{\partial}{\partial E}\left[E^3 F\right] + \left(\mu^2\left(\frac{\partial \ln \rho}{\alpha \partial t} + \frac{3u}{r}\right) - \frac{u}{r}\right)\frac{1}{E^2}\frac{\partial}{\partial E}\left[E^3 F\right], \end{aligned} \tag{8}$$

in a finite difference representation implementing the discrete ordinates, or S_N, method. The evolved quantity is the neutrino distribution function, $F(t, a, \mu, E)$, as a function of time t, rest mass a enclosed in a sphere at radius r, propagation angle cosine μ with respect to radial direction, and neutrino energy E. Neutrinos in specific beams are created and destroyed according to the collision term, C, which includes the interactions listed in Table 1. It is assumed that the neutrinos propagate freely between interactions. The free-particle motion along geodesics between collisions introduces the many correction terms apparent on the right hand side of Eq. (8). They stem from the use of spherical coordinates in combination with a description of the neutrino phase space in a comoving frame. Nevertheless, all terms can be labeled with a physical effect. In order of appearance in Eq. (8) these are, the time derivative of the neutrino distribution function, the propagation of neutrinos, the angle correction due to neutrino propagation, the angular aberration correction due to observer motion, the frequency shift in the gravitational potential, and the Doppler frequency shift due to observer motion. It is essential for the successful finite difference representation of Eq. (8) that it is upward compatible with simple special cases of the transport equation. Basic physical properties can be determined by the evaluation of expectation values with the neutrino distribution functions for various operators. The finite difference representation should support, e.g., the diffusion limit, total energy conservation, and the conservation of lepton number.

3.1.3. *Parameter settings*

Both runs, N13 and G15, have been performed with 103 adaptive spatial zones ranging from the center of the progenitor star to about 7000 km. A constant pressure boundary condition has been used at the barely moving surface. The neutrino energy has been resolved with 12 geometrically increasing energy groups in the range of $3 - 300$ MeV. The propagation angle has been discretized with 6 angles suitable for Gaussian Quadrature. Roughly 3000 time steps have been used for collapse and 7000 for the postbounce phase. The run N13 has been evolved with an order v/c approximation of Eqs. (2-8) and run G15 with the general relativistic equations.

3.2. VERTEX

Independently from the efforts of the Oak Ridge-Basel collaboration the Garching supernova group has approached the Boltzmann equation with a new variable Eddington factor method (Rampp 2000; Rampp & Janka 2000, 2002) for the neutrino transport in core-collapse supernovae and coupled it to the PROMETHEUS hydrodynamics code. The combined program allows for spherically symmetric (Rampp & Janka 2000, 2002) as well as multi-dimensional simulations (Janka et al. 2002; Buras et al. 2003). The spherically symmetric "core" of the program, which was used for the calculations described below, will be referred to by the name VERTEX (**V**ariable **E**ddington factor **R**adiative **T**ransfer for supernova **EX**plosions).

3.2.1. *Hydrodynamics*

The integration of the equations of hydrodynamics is performed with the Newtonian finite-volume code PROMETHEUS (Fryxell, Müller, & Arnett 1989) which was supplemented by additional problem specific features (Keil 1997). PROMETHEUS is a direct Eulerian, time-explicit implementation of the Piecewise Parabolic Method (PPM) of (Colella & Woodward 1984). As a second-order Godunov scheme with a Riemann solver it is particularly well suited for following discontinuities in the fluid flow like shocks or boundaries between layers of different chemical composition. A notable advantage is its capability of tackling multi-dimensional problems with high computational efficiency and numerical accuracy. The code makes use of the "Consistent Multifluid Advection (CMA)" method (Plewa & Müller 1999) for ensuring accurate advection of different chemical components in the fluid, and switches from the original PPM method to the more diffusive HLLE solver of Einfeldt (1988) in the vicinity of strong shocks to avoid spurious oscillations (the so-called "odd-even decoupling" phenomenon) when such shocks are aligned with one of the coordinate lines in multidimensional simulations (Quirk 1994; Kifonidis 2000; Plewa & Müller 2001).

3.2.2. *Neutrino transport*

The variable Eddington factor scheme for the neutrino transport, its coupling to the hydrodynamics part, and application to a number of test problems is described in much detail elsewhere (Rampp & Janka 2002). Here we will only briefly summarize the characteristic features of the method. The coupled set of equations of hydrodynamics (Eqs. (1)-(4) in (Rampp & Janka 2002)) and radiation transport (Eqs. (6)-(8) ibidem) is equivalent to Eqs. (2)-(7) in the order (v/c) limit. The equations are also split into a "hydrodynamics part" and a "neutrino part" and solved independently in subsequent ("fractional") steps. But the hydrodynamics and the transport solver can use radial grids and/or time steps that are different from each other.

In the neutrino transport method the integro-differential character of the Boltzmann equation is tamed by applying a variable Eddington factor closure to the neutrino energy and momentum equations (and the simultaneously integrated first and second order moment equations for neutrino number). For this purpose the variable Eddington factor is determined from the formal solution of the Boltzmann equation on so-called "tangent rays". They coincide with radiation characteristics in Newtonian geometry. The system of the Boltzmann equation and its moment equations is iterated until convergence is achieved. The integration of the transport equations is implicit in time.

General relativistic effects are treated only approximately in the code (Rampp & Janka 2002). The current version contains a modification of the gravitational potential by including correction terms due to pressure and energy of the stellar medium and neutrinos, which are deduced from a comparison of the Newtonian and relativistic equations of motion. The neutrino transport contains gravitational redshift and time dilation, but ignores the distinction between coordinate radius and proper radius. This simplification is necessary for coupling the transport code to the basically Newtonian hydrodynamics. We shall demonstrate in this paper that these approximations seem to work satisfactorily well (see Sect. 4.2), at least as long as there are only moderate (∼10–20%) deviations of the metric coefficients from unity and the infall velocities do not reach more than 10–20% of the speed of light in decisive phases of the evolution.

3.2.3. *Parameter settings*

For the neutrino transport in the N13 run an Eulerian radial grid with 234 radial zones (254 tangent rays) spaced logarithmically between 0 and 10 000 km was used. The neutrino spectrum between 0 and 380 MeV was discretized with 21 geometrically zoned energy bins, the center of the first bin being located at 2 MeV. The hydrodynamics, on the other hand, was solved on a radial grid of 400 zones which are moved with the stellar fluid during core collapse. Shortly after core bounce both radial grids were rezoned such that inside of a radius of 400 km the zones of the transport grid coincide with those of the hydro grid. For the post-bounce evolution the coordinates of the hydrodynamic grid (as well as those of the transport grid) remained fixed in time. Concerning the resolution and definition of numerical grids the same parameters were chosen in the G15 run with the exception that 17 energy bins between 0 and 380 MeV were used instead of 21 groups.

4. COMPARISON OF THE RESULTS

The detailed simulations produce a sizeable amount of data, even if they are confined to one spatial dimension. Hence, we start with an overview of what we are going to compare and how the comparable quantities are derived from the code-specific results. During collapse and bounce it is quite natural to choose the enclosed baryon mass as spatial coordinate. It labels individual fluid elements and allows the presentation of the evolution history of each fluid element. Some tenths of milliseconds after bounce, the configuration becomes rather stationary in radius and the presentation of the quantities as a function of radius is more interesting. We will present the density, entropy per baryon, electron fraction, and velocity of the stellar fluid; and the neutrino luminosities and rms energies as a function of the spatial coordinate. Also interesting are selected quantities as functions of time, e.g. the trajectories of fluid elements, the shock position, the central conditions, or the neutrino luminosities and rms energies sampled at 500 km radius (as an approximation to radial infinity). The physical time in both runs is synchronized at bounce ($t = 0$), the moment when the central density reaches a local maximum immediately before the shock is formed. We define the shock position by the maximum in the velocity divergence (i.e. maximum compression, cf. Eq. (2)),

$$R_s = \max_r \left(-\frac{\partial(4\pi r^2 u)}{\partial V} \right).$$

The luminosities and rms energies are given in the comoving frame as a function of the neutrino phase-space distribution function $F(t, a, \mu, E)$ according to

$$L(t,a) = \int F(t,a,\mu,E) E^3 dE \mu d\mu$$

$$\langle \epsilon(t,a) \rangle_{rms} = \sqrt{\int F(t,a,\mu,E) E^4 dE d\mu / \int F(t,a,\mu,E) E^2 dE d\mu}.$$

We compare time slices in our runs at three different typical instances in the postbounce evolution: Bounce ($t_{pb} = 0$ ms), burst ($t_{pb} = 3$ ms), and broil ($t_{pb} > 100$ ms).

4.1. *Newtonian 13 $M_\odot$ Model*

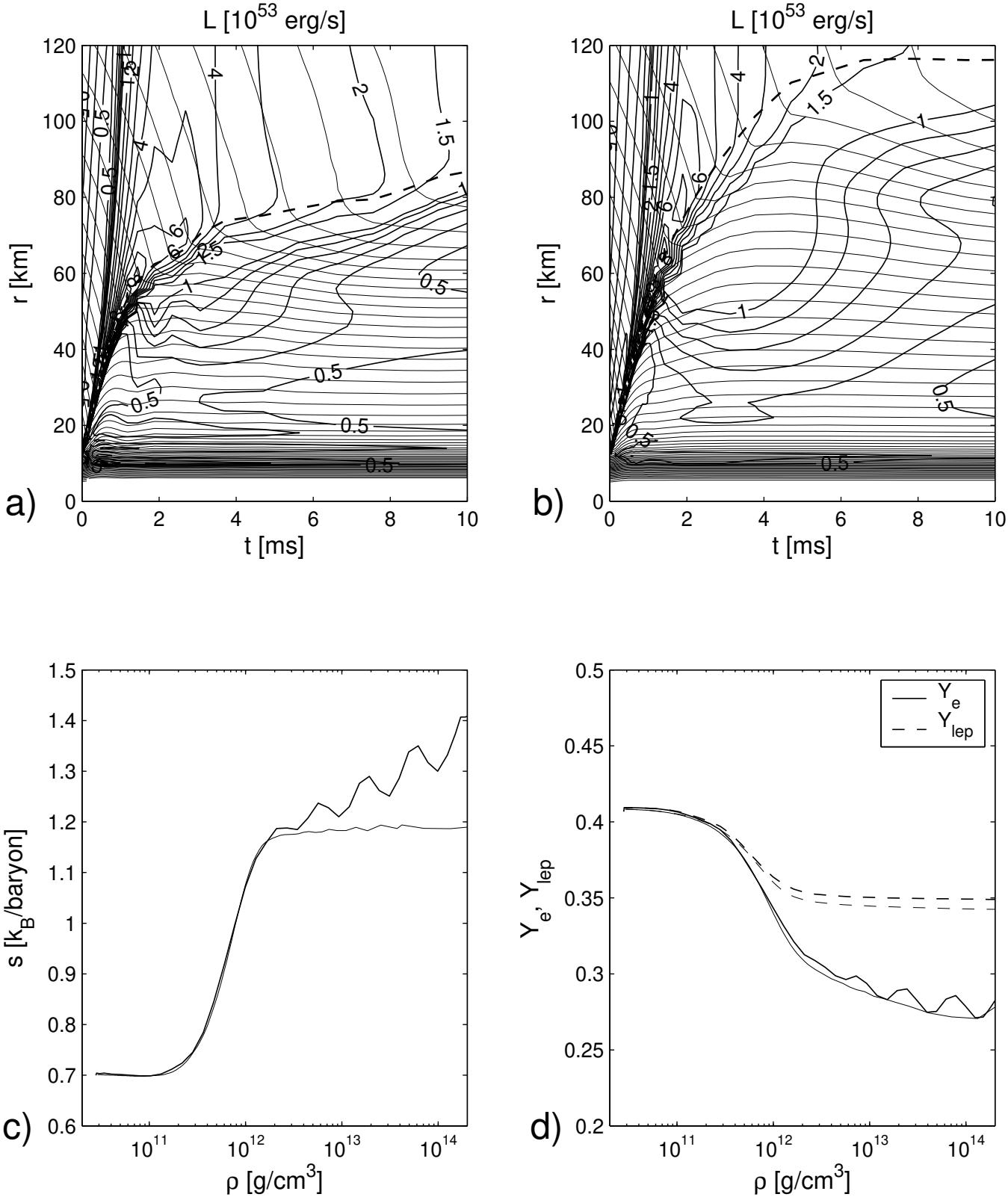

FIG. 1.— Graph (a) shows the first 10 ms after bounce for model N13 in the simulation with AGILE-BOLTZTRAN. Graph (b) shows the same time period in the simulation with VERTEX. The thin lines represent trajectories of fluid elements spaced with an interval of 0.02 $M_\odot$. The thicker contour lines indicate the luminosity as a function of radius and time. The dashed line marks the shock position as a function of time. We note a small rarefaction wave in graph (a) that is caused at about 1 ms after bounce by the settling of matter in the gravitational potential after the first dynamic re-expansion. It reaches the shock during the neutrino burst at about 3 ms after bounce. It leads to a luminosity dip that can be seen to propagate outward, with sound speed inside the shock position and with speed of light outside the shock position. In graph (b), we see a more quickly decaying neutrino burst launched from a more dynamical shock. The mass trajectories indicate an expansion behind the shock lasting for more than 4 ms. This is the time the shock takes to turn into an accretion shock in the VERTEX simulation. Graph (c) compares the entropy of the innermost zone as a function of density in AGILE-BOLTZTRAN (thick line) and in VERTEX (thin line). The agreement before trapping is close to perfect, dynamically insignificant differences appear at larger densities. Graph (d) shows an analogous comparison for the electron fraction (solid lines) and lepton fraction (dashed lines) in the innermost zone.

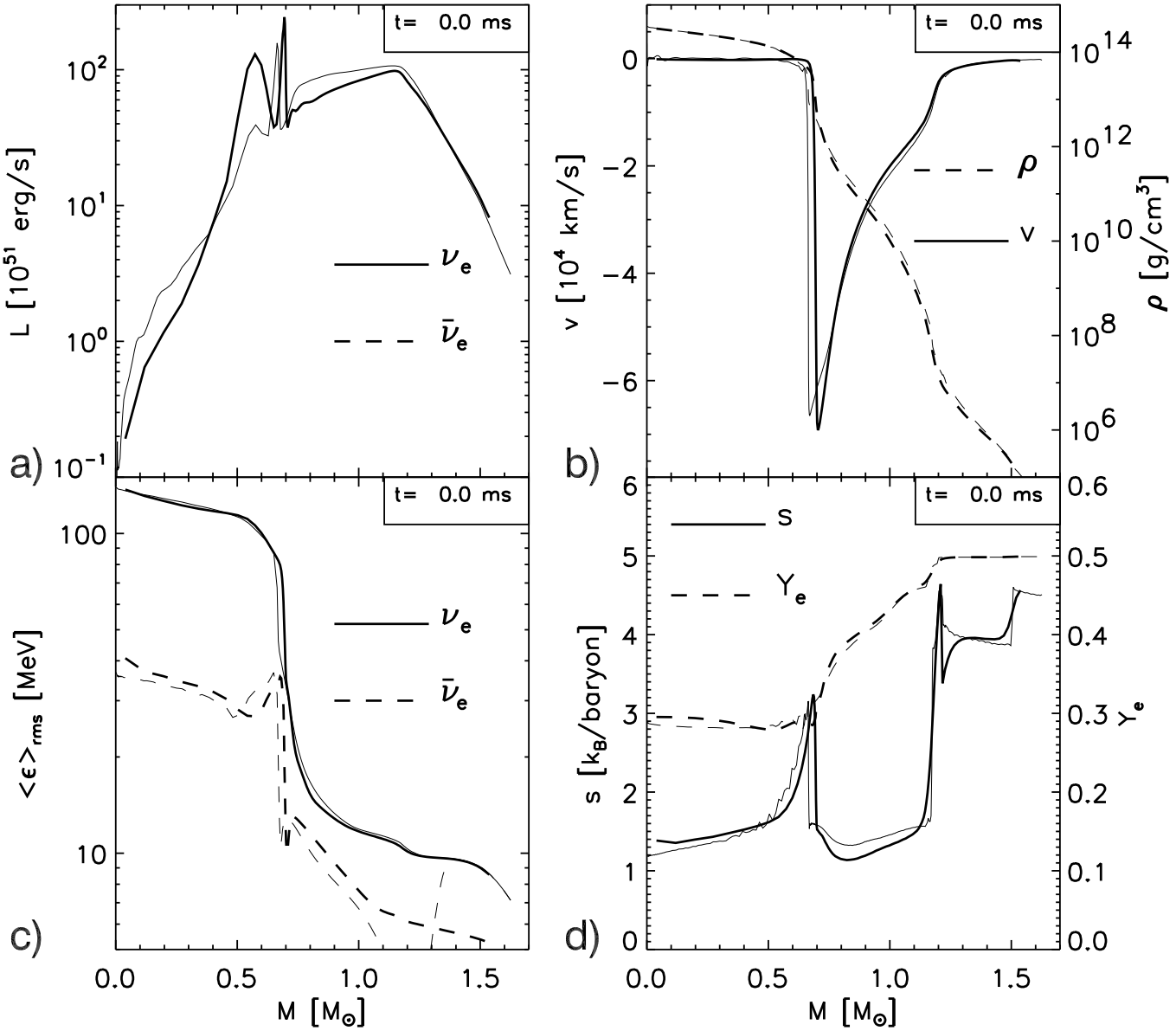

FIG. 2.— Snapshot at bounce for model N13. Data from the AGILE-BOLTZTRAN simulation are drawn with a thick line. Data from the VERTEX simulation are drawn with a thin line. Graph (b) shows the velocity (solid lines) and density (dashed lines) profiles, graph (d) the entropy (solid lines) and electron fraction (dashed lines). The neutrino luminosities are given in graph (a) and the neutrino rms energies in graph (c). Solid lines refer to electron neutrinos and dashed lines to electron antineutrinos. The central electron fraction in VERTEX is smaller than in AGILE-BOLTZTRAN and the shock forms at a slightly smaller enclosed mass. The luminosities in AGILE-BOLTZTRAN are mostly smaller than in VERTEX. The higher values around an enclosed mass of 0.5 $M_\odot$ may be explained by a lower opacity for coherent scattering around the phase transition to bulk nuclear matter.

We start the comparison with an investigation of differences in the N13 run. Fig. 1 shows the mass trajectories for both runs around bounce; in graph (a) for AGILE-BOLTZTRAN and in graph (b) for VERTEX. The rising dashed line marks the shock position. The first inspection reveals a difference of 30% in shock radius at 7 ms after bounce. This early appearance of a discrepancy is quite unfortunate for our purpose because the runs diverge at this point in a way that makes an accurate comparison in later phases more difficult.

We interpret the conditions at bounce by first looking at the luminosities in Fig. 2, graph (a). We find of order 25% higher luminosities in VERTEX around an enclosed mass of 0.2 $M_\odot$ and 0.8 $M_\odot$, while the luminosity in AGILE-BOLTZTRAN is by a factor of two larger around 0.5 $M_\odot$. The neutrino rms energies in graph (c) exhibit good agreement.

In the diffusive regime they reflect the temperature profiles, which are linked to the entropy profiles shown in graph (d). The differences in the electron fraction in graph (d) are of order 5%, the differences in the neutrino abundances are even smaller. Most of these differences are introduced during the last 2 ms before bounce. The profiles are in close to perfect agreement beforehand. For example, this becomes evident in graphs (c) and (d) of Fig. 1 where we plotted the entropy and lepton fractions of the innermost zone as functions of density during core collapse. We find that most of the deleptonization difference is produced at a density just before trapping, when the effective electron capture rates are highest.

The entropy evolution shows perfect agreement during infall, but after neutrino trapping, an unphysical entropy increase in the innermost zones takes place in the AGILE-BOLTZTRAN simulation. The wiggles in the evolution of the electron fraction and entropy in AGILE-BOLTZTRAN are caused by limited resolution of the neutrino Fermi energy as explained in detail in (Mezzacappa & Bruenn 1993b). The entropy difference in the innermost zones can also be seen in graph (d) of Fig. 2. The entropy in VERTEX around the position of shock formation has increased slightly during the last millisecond before bounce whereas the entropy in AGILE-BOLTZTRAN in these zones sinks. This leads to small differences in the entropy of the infalling material. A resolution study in (Liebendörfer et al. 2004) demonstrates that a part of this difference is related to the adaptive grid rushing inwards to resolve the shock front when the pressure wave launched at bounce steepens up at the sonic point. Simulations with higher spatial resolution would be closer to the VERTEX results in this particular moment. The artificial diffusion associated with the dynamical adaptive grid also makes the transition at composition boundaries in the outer layers of the progenitor smoother than the sharp step functions seen in VERTEX. However, these differences at bounce are small and are not expected to have significant influence on the dynamics in the following phases, although some differences in the model structure can be caused.

The velocity profiles in graph (b) of Fig. 2 are consistent with the thermodynamical conditions. The smaller electron fraction in VERTEX leads to a 3% smaller enclosed mass at shock formation. The infall velocities in the outer core are smaller in AGILE-BOLTZTRAN. The density profiles shown in the same graph demonstrate the expected higher values where the support by electron pressure is lower, and agree very well otherwise. In summary there are visible differences at bounce, but none of them is alarmingly large or an obvious cause for large deviations in the postbounce evolution. We also note that the evolution of the discussed quantities in both runs deliver an in itself perfectly coherent picture.

The next moment of comparison is at 3 ms after bounce. This instance is interesting because this is the time when the shock positions in the two codes start to deviate in Fig. 1. There we find in VERTEX a continued expansion of the shock radius until the density behind the shock reaches values around $10^{10.5}$ g/cm^3. The shock radius in AGILE-BOLTZTRAN shows a kink after 2 ms and does not become as large as in VERTEX. The density behind the shock rather remains around $10^{11.5}$ g/cm^3. The origin of this discrepancy lies in a stronger shock in VERTEX as cause and a different neutrino burst behavior as consequence and amplification mechanism. The bounce-shock is dynamic at the beginning and drives matter outwards with positive velocities. However, as the shock dissociates the infalling material and neutrino losses become important, it loses its kinetic energy and converts into an accretion shock. The accretion shock is characterized by a velocity jump that connects the high speed/low density infalling material to the shocked low speed/high density region behind the shock. There is an important difference between the dynamic and the accretion shock. The material behind the dynamic shock expands while the material behind an accretion shock continues to be compressed. By examining the mass trajectories, one finds that VERTEX maintains a dynamic shock for a much longer time than AGILE-BOLTZTRAN. In AGILE-BOLTZTRAN the expanding mass elements behind the shock turn around very soon and form a rarefaction wave that catches up with the shock. In contrast, the mass elements behind the dynamic shock in VERTEX stay in collective expansion for a more extended period of time.

This difference in shock propagation is initially not very large. It is dramatically amplified by the coincidence of the electron neutrino burst with the transition from a dynamic to an accretion shock. As the shock compresses the infalling lepton-rich material, the fermionic electrons have to populate high energy levels and are rapidly converted to neutrinos by captures on protons, provided the produced neutrinos can escape from the region behind the shock such that the Fermi blocking in the neutrino phase space does not establish kinetic equilibrium by an equally strong reverse reaction. It makes a significant difference, if this density is reached by the shock in a dynamical or accretion phase. If the neutrino burst is launched from a dynamical phase, infalling matter deleptonizes due to the immediate compression while crossing the shock front. After that, electron captures are reduced quickly as the matter re-expands behind the dynamical shock and the density drops again. Moreover, the dynamic shock continues to propagate outwards into smaller densities and accretion rates such that the emission from the shock front also decreases. In an accretion shock, the infalling matter experiences the same initial deleptonization in the shock front and continues to emit neutrinos due to the compression behind the shock. The neutrino burst from an accretion shock is therefore more intensive. The neutrino emission behind the shock removes energy and lepton number and reduces the pressure support. Therefore the density behind the shock almost locks in. Thus, electron captures continue at high densities and the neutrino signal decays less quickly. The different interplay between shock propagation and neutrino burst can be seen in the luminosity contour lines in Fig. 1. We find a very similar initial peak and then a much slower decay due to the accretion shock in the AGILE-BOLTZTRAN calculation than in the VERTEX run with the dynamic shock. The cropped peak in the AGILE-BOLTZTRAN signal is caused by the additional coincidence of the rarefaction wave reaching the accretion shock from behind and transiently reducing the shock strength.

After these explanations we can easily interpret the time slice at 3 ms after bounce presented in Fig. 3. In the luminosity, graph (a), we see good agreement in the launch of the neutrino burst. The differences discussed in the bounce time slice have been reduced, but are still visible. The slightly higher rms energies of the burst electron neutrinos, compared to the previously emitted ones, are visible in graph (c). The entropy profiles and electron fraction

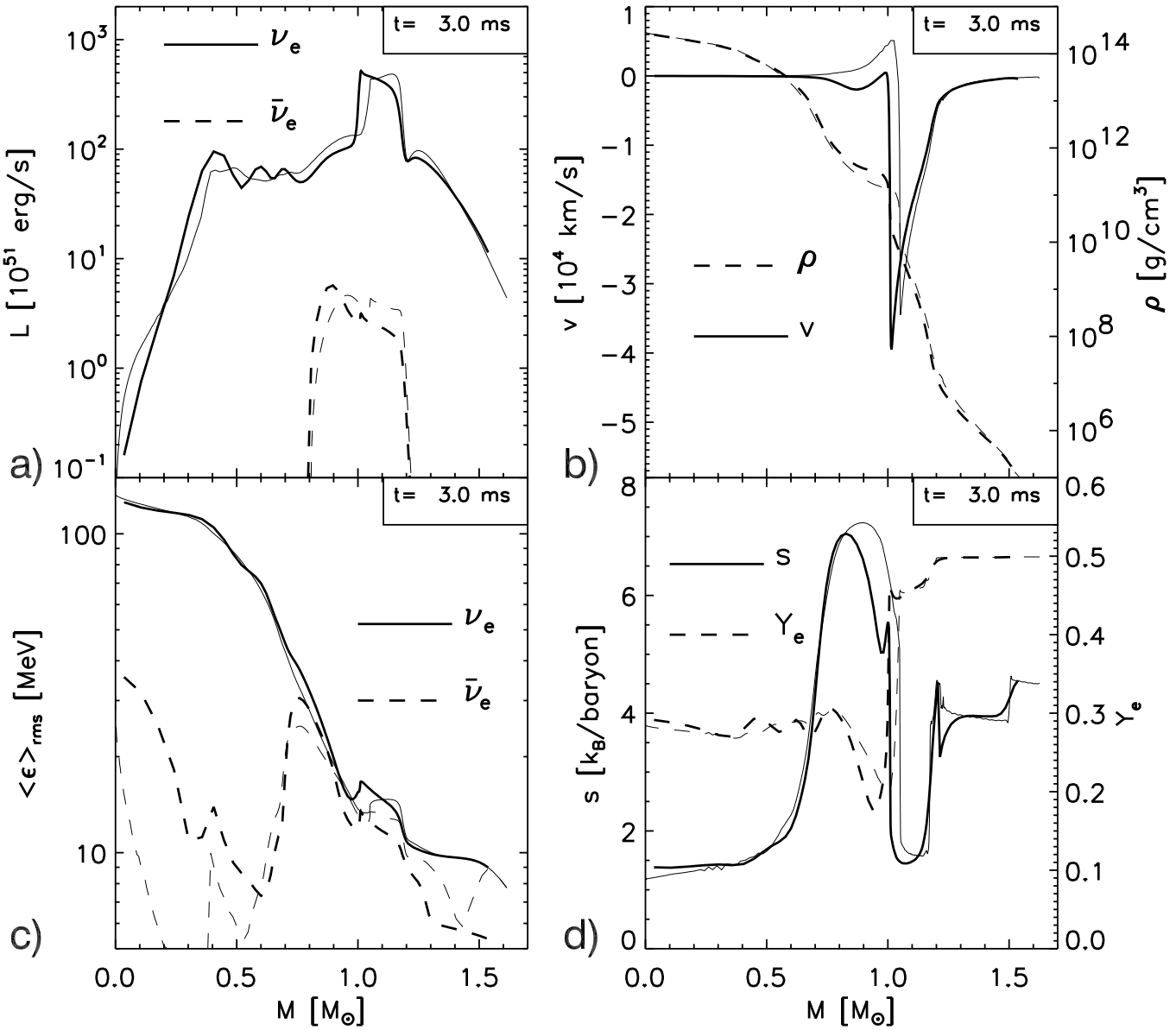

FIG. 3.— Snapshot at 3 ms after bounce for model N13. Data from the AGILE-BOLTZTRAN simulation are drawn with a thick line. Data from the VERTEX simulation are drawn with a thin line. Graph (b) shows the velocity (solid lines) and density (dashed lines) profiles, graph (d) the entropy (solid lines) and electron fraction (dashed lines). Graph (a) and (c) show the neutrino luminosities and rms energies respectively. Solid lines refer to electron neutrinos and dashed lines to electron antineutrinos. An outrunning rarefaction wave is just about to reach the accretion shock in the AGILE-BOLTZTRAN simulation whereas the propagating shock in the VERTEX simulation still has kinetic energy.

profiles in graph (d) demonstrate the different location and progression of the electron neutrino burst as discussed above. In AGILE-BOLTZTRAN the entropy and electron fraction drops to a minimum at a smaller enclosed mass and the deleptonization in AGILE-BOLTZTRAN is more pronounced than in VERTEX because of the different compression rate of the material behind the shock. The higher density behind the shock can clearly be made out in graph (b). The same graph shows the velocity profiles where the higher kinetic energy of the dynamic VERTEX shock becomes evident. The shock in AGILE-BOLTZTRAN has already transformed to an accretion shock and the outgoing rarefaction wave from the recontraction is just about to reach the shock position.

The further evolution is best seen in the time-dependent diagrams in Fig. 4. In graph (b), the luminosities and

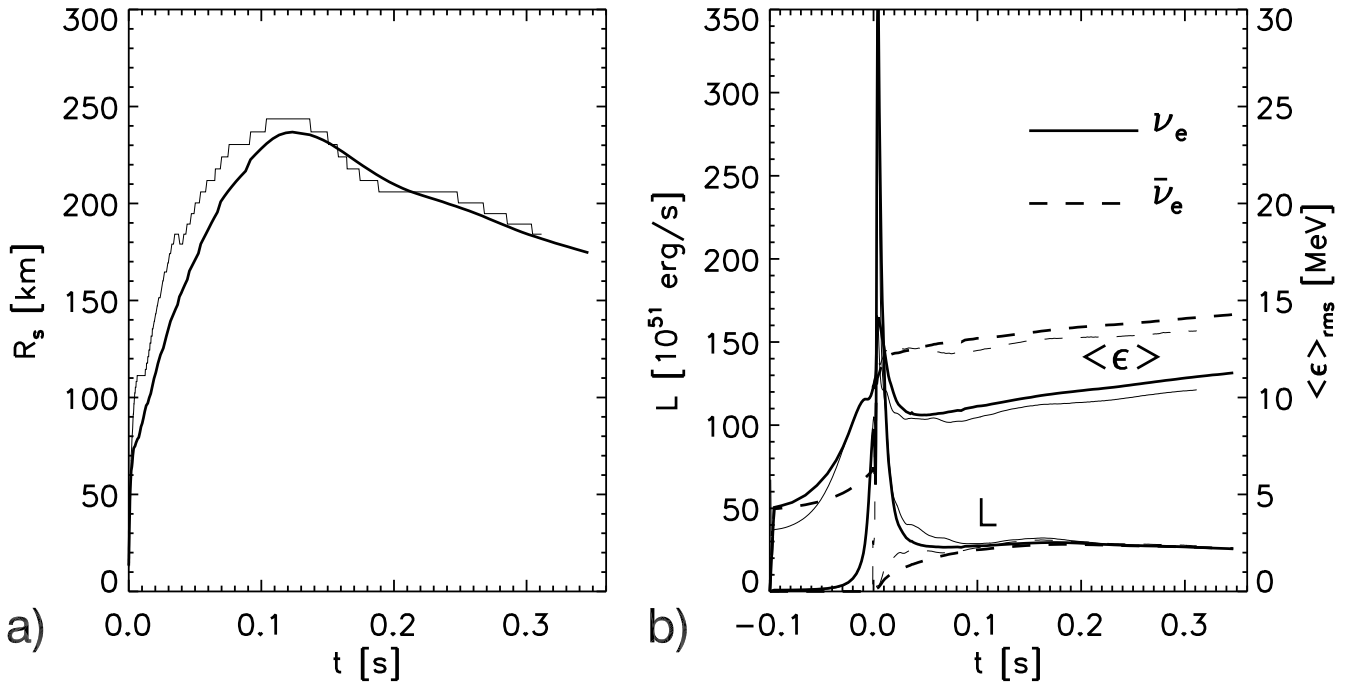

FIG. 4.— The shock position as a function of time for model N13 is shown in graph (a). The shock in VERTEX (thin line) propagates initially faster and converges after maximum nicely to the position of the shock in AGILE-BOLTZTRAN (thick line). The neutrino luminosities and rms energies for model N13 are presented as functions of time in graph (b). The values are sampled at a radius of 500 km in the comoving frame. The solid lines belong to electron neutrinos and the dashed lines to electron antineutrinos. The line width distinguishes between the results from AGILE-BOLTZTRAN and VERTEX in the same way as in graph (a). The luminosity peaks are nearly identical, the rms energies are tendentially larger in AGILE-BOLTZTRAN.

rms energies are shown, sampled at a fixed radius of 500 km. The two neutrino signals are qualitatively very similar. The neutrino burst is nearly identical and deviations are maximally 20% around 50 ms after bounce. This difference is a late consequence of the deleptonization differences during the neutrino burst. The material in VERTEX is left with higher electron fraction and higher entropy behind the neutrino burst. Hence it deleptonizes at a higher rate afterwards. The rms energies tend to be lower in VERTEX than in AGILE-BOLTZTRAN. Finally, graph (a) compares the shock trajectories over a longer period of time. We find the described differences in the initial shock propagation and excellent agreement afterwards in the steady-state accretion phase. The maximum shock radius deviates only by 5%.

We finish the comparison of the N13 model with a closer look at a time slice at 150 ms after bounce. A snapshot of this quasi-stationary accretion phase is shown in Fig. 5. Graph (a) demonstrates agreement of the luminosities in the inner diffusive part of the protoneutron star. The rms energies in graph (c) agree equally well. Around the neutrinospheres, VERTEX seems to emit neutrinos more copiously than AGILE-BOLTZTRAN. The higher densities in VERTEX around a radius of 100 km in graph (b) together with the close agreement in the infall velocities points to a smaller accretion rate in AGILE-BOLTZTRAN. This is consistent with the described luminosity differences. The rms energies in VERTEX are slightly lower in the gain region. At the gain radius, neutrino emission and neutrino absorption are in balance. The lower entropy in VERTEX visible in graph (d) may cause the lower rms energies of the emitted neutrinos at this position. The larger density in the VERTEX profile also favors a lower electron fraction in weak equilibrium. The preferential absorption of electron antineutrinos is therefore more pronounced in the heating region of VERTEX than in the heating region of AGILE-BOLTZTRAN. The observation that the lower entropy and lower electron fraction in VERTEX ~ 100 km radius is again consistent with the larger density closes the cycle without pinpointing a cause of the differences in this stationary phase with strong couplings among the different quantities. At least the differences in the entropy profiles could be caused by the entropy differences found in the infalling material. The transiently higher pre-shock entropy in the AGILE-BOLTZTRAN simulation at 150 ms after bounce could translate into lower density and less deleptonization behind the shock.

4.2. *General Relativistic 15 $M_\odot$ Model*

Let us again start with the conditions at bounce. The evolution of the entropy and lepton fraction in the innermost zone in graphs (c) and (d) of Fig. 6 does not provide new insight with respect to our description in the N13 case, except for the final value of the entropy, which is now clearly smaller in AGILE-BOLTZTRAN, and the final value of the electron fraction, which is smaller in VERTEX. This effect can also be inferred from the time slice at bounce in graph (d) of Fig. 7. The higher central entropy and lower central electron fraction are a consequence of the inclusion of ion-ion correlations in the VERTEX simulations. The differences are consistent with the values determined in (Bruenn &

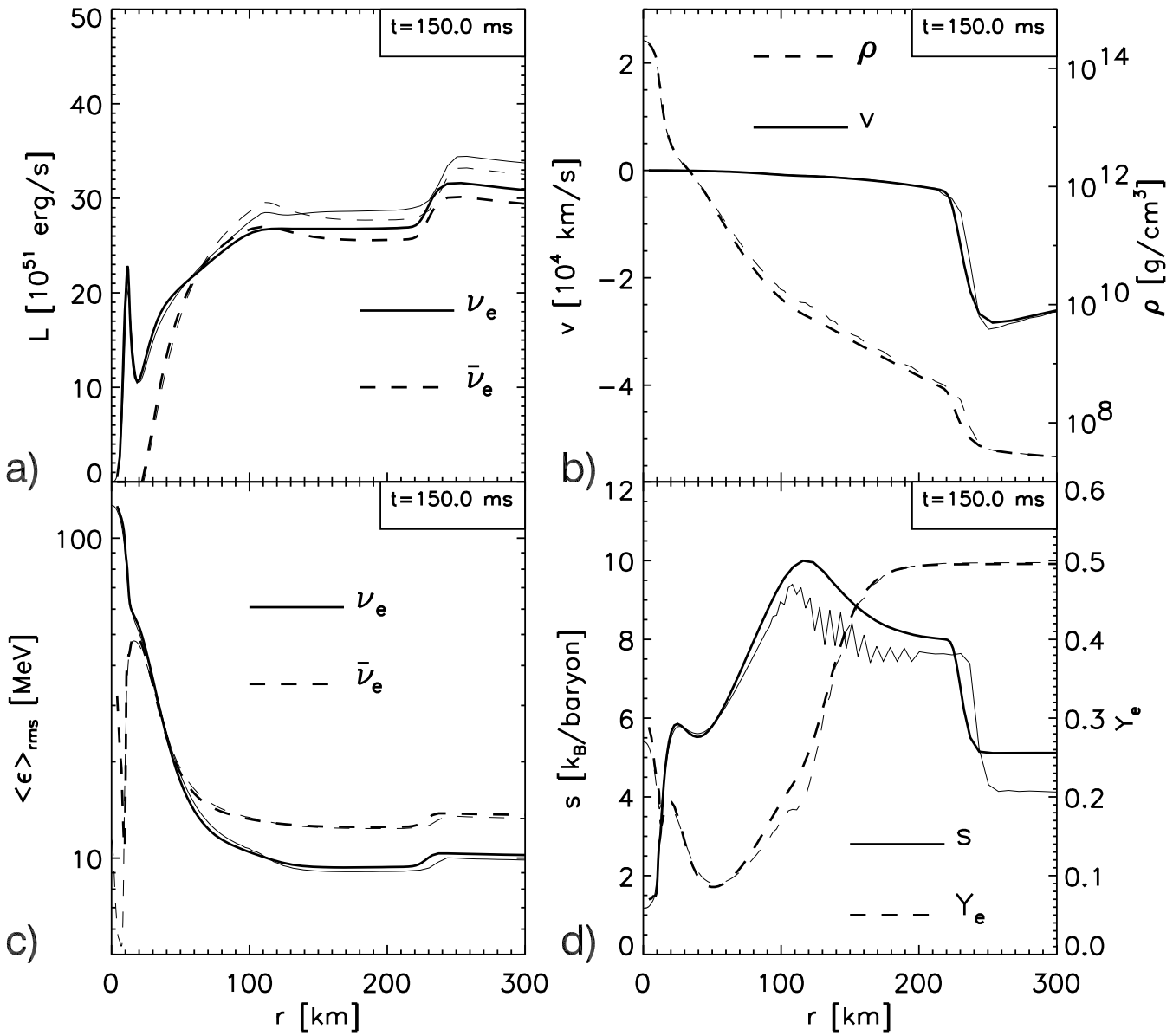

FIG. 5.— Snapshot at 150 ms after bounce for model N13. Data from the AGILE-BOLTZTRAN simulation are drawn with a thick line. Data from the VERTEX simulation are drawn with a thin line. Graph (b) shows the velocity (solid lines) and density (dashed lines) profiles, graph (d) the entropy (solid lines) and electron fraction (dashed lines). The neutrino luminosities and rms energies are shown in graphs (a) and (c) respectively. Solid lines refer to electron neutrinos and dashed lines to electron antineutrinos. This stationary-state situation is critical for neutrino heating on a longer time scale. The agreement is very close in most quantities.

Mezzacappa 1997; Rampp 2000). The exact agreement of the central entropy in Fig. 7d is a coincidental interference of the mentioned entropy difference with the numerical entropy drift in AGILE-BOLTZTRAN described in the N13 model. The luminosities in graph (a) of Fig. 7 show again a higher preshock luminosity in VERTEX and reasonable agreement in the diffusive interior regions.

Almost paradoxically we find better agreement for the postbounce evolution in our relativistic run, G15, than in the previously discussed N13 run. This is the case despite the fact that the progenitor data have not been matched, the microphysics ingredients are not exactly the same (VERTEX includes ion-ion screening and nucleon-nucleon bremsstrahlung, AGILE-BOLTZTRAN does not) and general relativistic effects are included selectively in VERTEX and comprehensively in AGILE-BOLTZTRAN. The main reason is the much weaker bounce shock. General relativistic effects

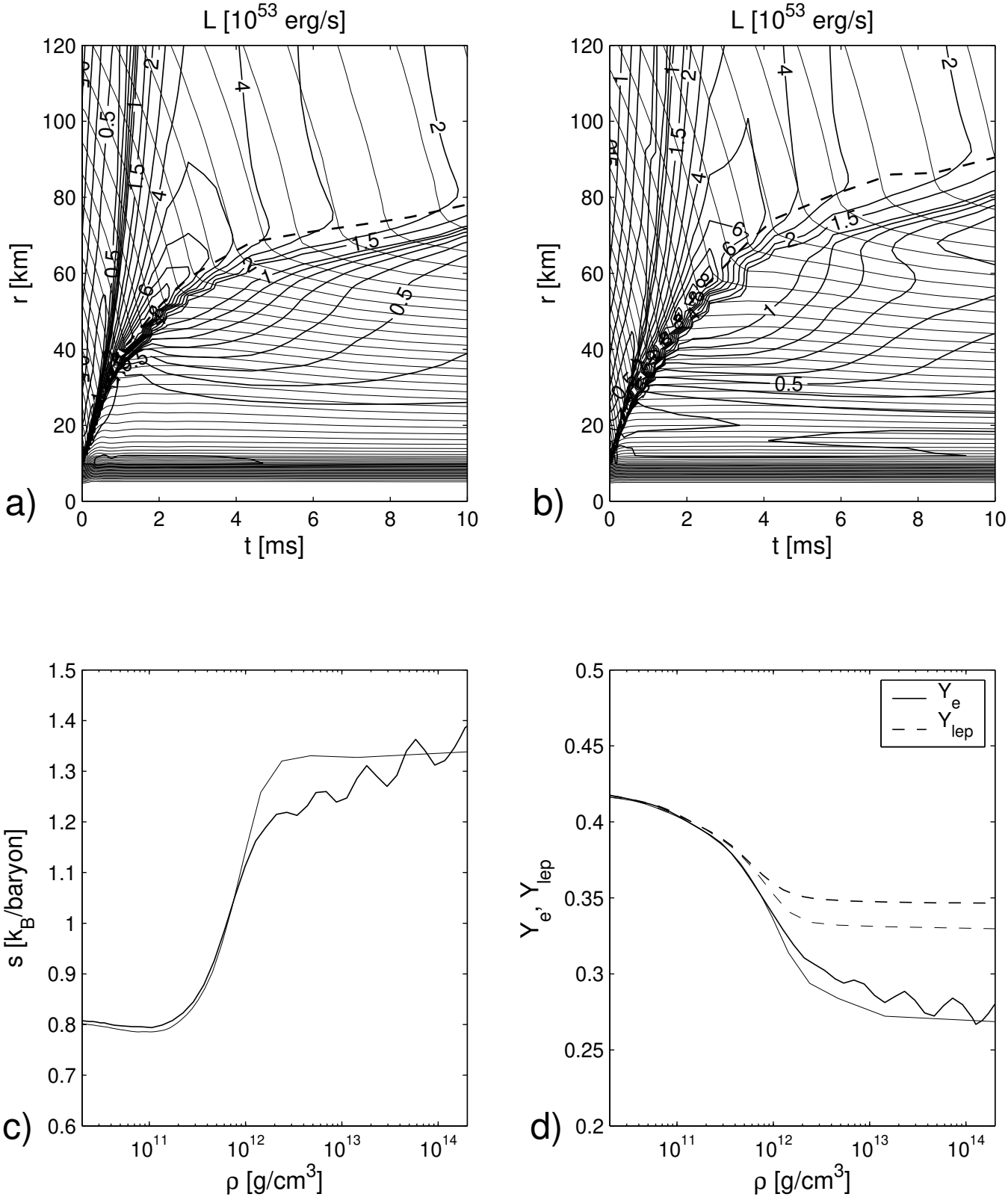

FIG. 6.— Graph (a) shows the first 10 ms after bounce for model G15 in the simulation with AGILE-BOLTZTRAN. Graph (b) shows the same time period in the simulation with VERTEX. The thin lines represent trajectories of fluid elements spaced with an interval of 0.02 $M_\odot$. The thicker contour lines indicate the luminosity as a function of radius and time. The dashed line marks the shock position as a function of time. We find a very similar extended neutrino burst in the simulations with both methods. Under consideration of general relativistic effects and the emission of μ- and τ-neutrinos, the shock turns into an accretion shock earlier, before or right at the release of the neutrino burst. Graph (c) compares the entropy of the innermost zone as a function of density in AGILE-BOLTZTRAN (thick line) and in VERTEX (thin line). The agreement before trapping is close to perfect, dynamically insignificant differences appear at larger densities. Graph (d) shows an analogous comparison for the electron fraction (solid lines) and lepton fraction (dashed lines) in the innermost zone. Differences in the input physics explain the slightly larger differences found in the G15 run than in the N13 run.

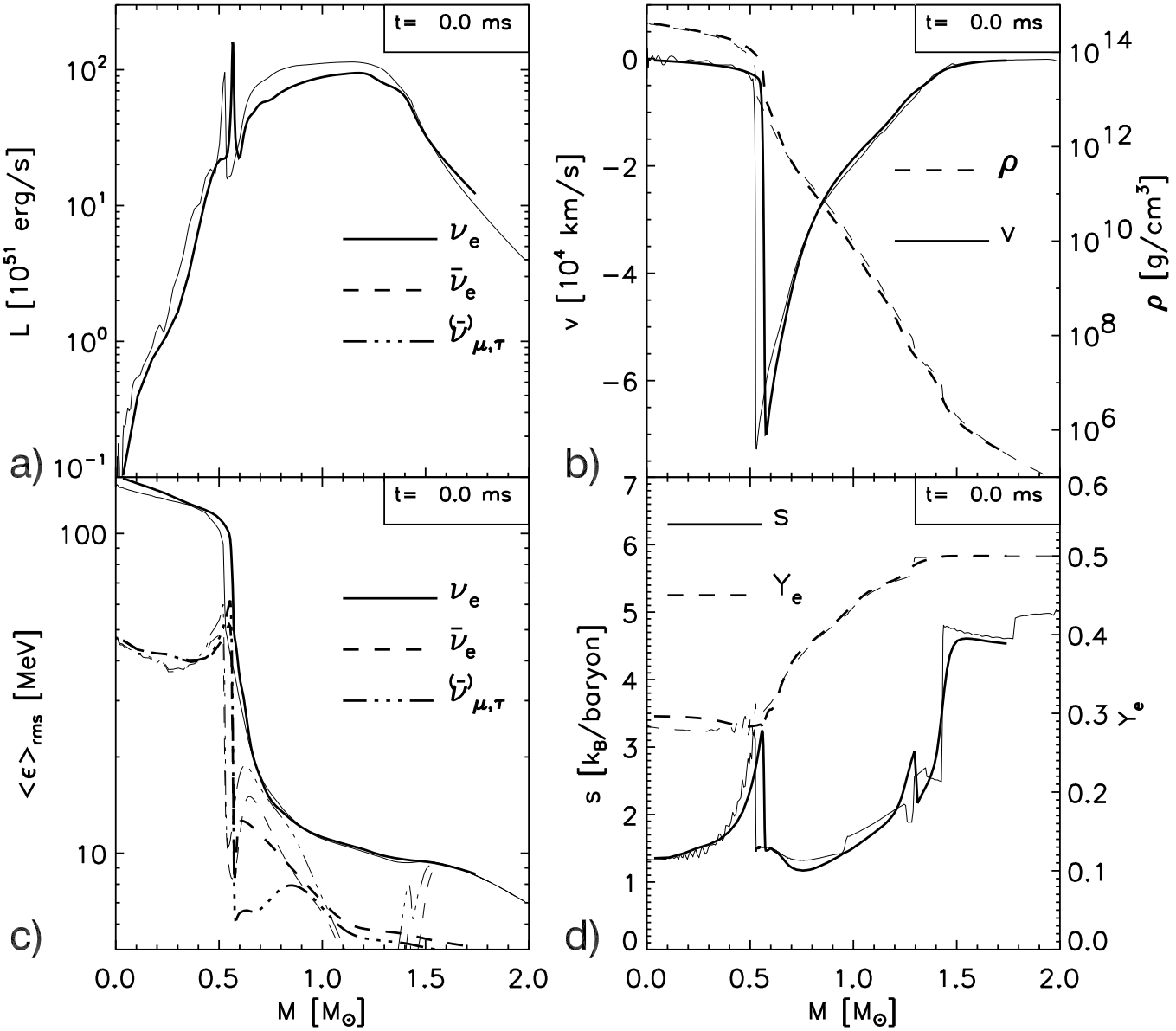

FIG. 7.— Snapshot at bounce for model G15. Data from the AGILE-BOLTZTRAN simulation are drawn with a thick line. Data from the VERTEX simulation are drawn with a thin line. Graph (b) shows the velocity (solid lines) and density (dashed lines) profiles, graph (d) the entropy (solid lines) and electron fraction (dashed lines). The neutrino luminosities and rms energies are shown in graphs (a) and (c) respectively. Solid lines refer to electron neutrinos, dashed lines to electron antineutrinos, and dash-dotted lines to μ- or τ-neutrinos (or their antiparticles). The luminosities in AGILE-BOLTZTRAN are mostly smaller than in VERTEX, whereas the central electron fraction and the enclosed mass at shock formation are slightly larger in AGILE-BOLTZTRAN.

during core collapse shift the sonic point to a 20% smaller enclosed mass and lead to a less energetic bounce shock (e.g. (Liebendörfer et al. 2001)) which has to dissociate more infalling material. The inclusion of μ- and τ-neutrinos in the G15 runs additionally leads to energy losses from the region behind the shock. As the shock loses its kinetic energy quickly in both G15 runs, the electron neutrino bursts are launched from the accretion shock phase. Hence it does not come to the discussed effect of a shorter electron neutrino burst which was favorable for the prompt shock expansion in the VERTEX run of model N13. Graphs (a) and (b) of Fig. 6 demonstrate extended neutrino bursts that look very similar. They both compare well with the AGILE-BOLTZTRAN N13 extended burst of Fig. 1. In the present case, the AGILE-BOLTZTRAN shock is stronger during the first 3 ms after bounce and somewhat weaker afterwards.

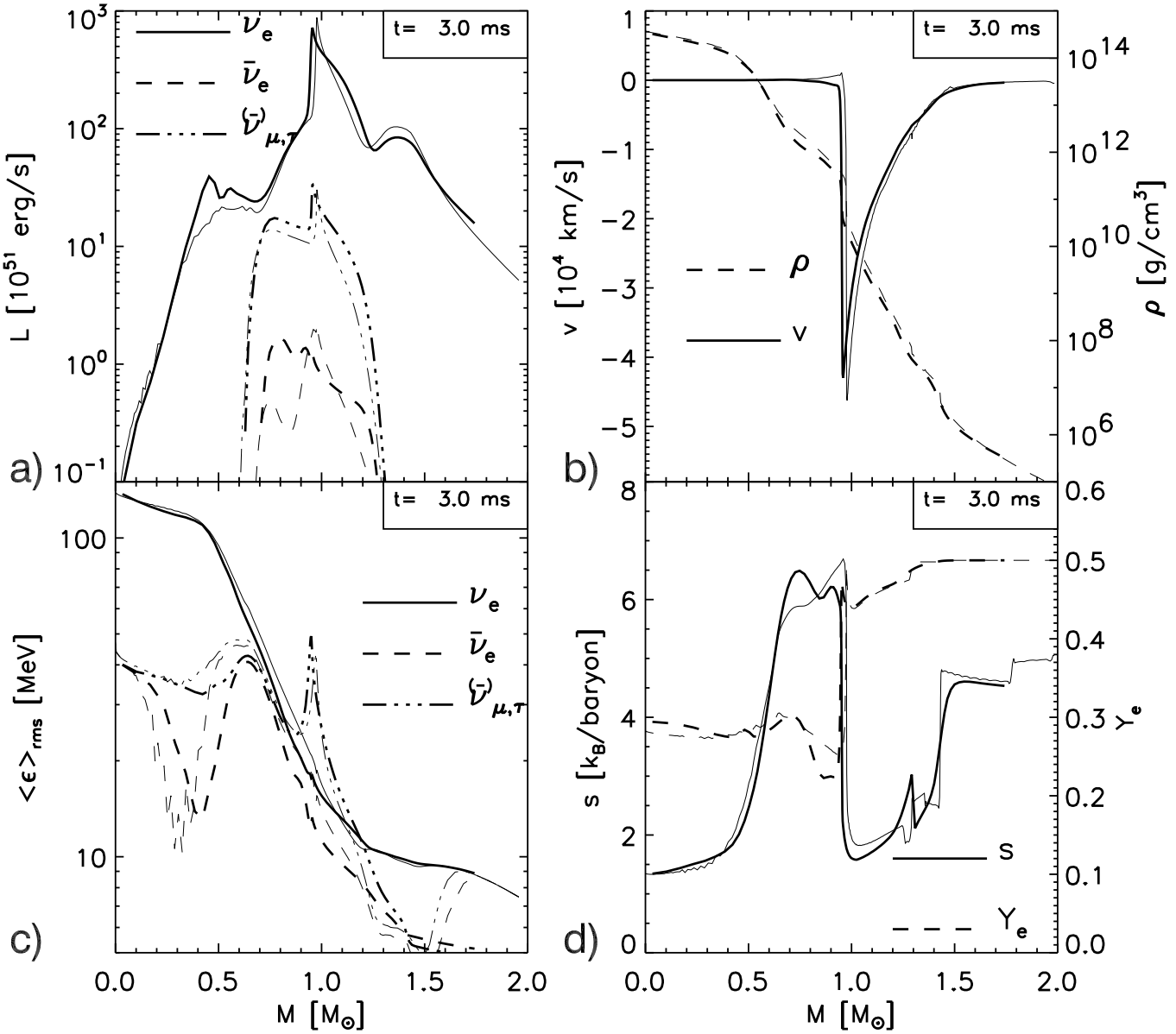

FIG. 8.— Snapshot at 3 ms after bounce for model G15. Data from the AGILE-BOLTZTRAN simulation are drawn with a thick line. Data from the VERTEX simulation are drawn with a thin line. Graph (b) shows the velocity (solid lines) and density (dashed lines) profiles, graph (d) the entropy (solid lines) and electron fraction (dashed line). The neutrino luminosities and rms energies are shown in graphs (a) and (c) respectively. Solid lines refer to electron neutrinos, dashed lines to electron antineutrinos, and dash-dotted lines to μ- or τ-neutrinos (or their antiparticles). Variations in the entropy profiles reflect the differences in the shock strength during the different propagation phases. The deleptonization by the neutrino burst occurs an instant earlier in the AGILE-BOLTZTRAN simulation.

The initially stronger phase is consistent with the finding that the shock formation in VERTEX takes place at a smaller enclosed mass (see Fig. 7b) because of the smaller core electron fraction shown in Fig. 7d. The slightly weaker shock in AGILE-BOLTZTRAN after 3 ms is compatible with the generally weaker shock propagation in AGILE-BOLTZTRAN, which we have already noticed in the N13 model.

The neutrino luminosities at 3 ms after bounce in Fig. 8, graph (a), do not reveal new features, except for the presence of μ- and τ-neutrinos that had not been included in the N13 run. Because of the absence of charged-current reactions of these neutrinos, they decouple at higher densities and reach appreciable luminosities earlier in the evolution, before the appearance of electron antineutrinos. The velocity profiles are very similar at 3 ms after bounce (confirming the

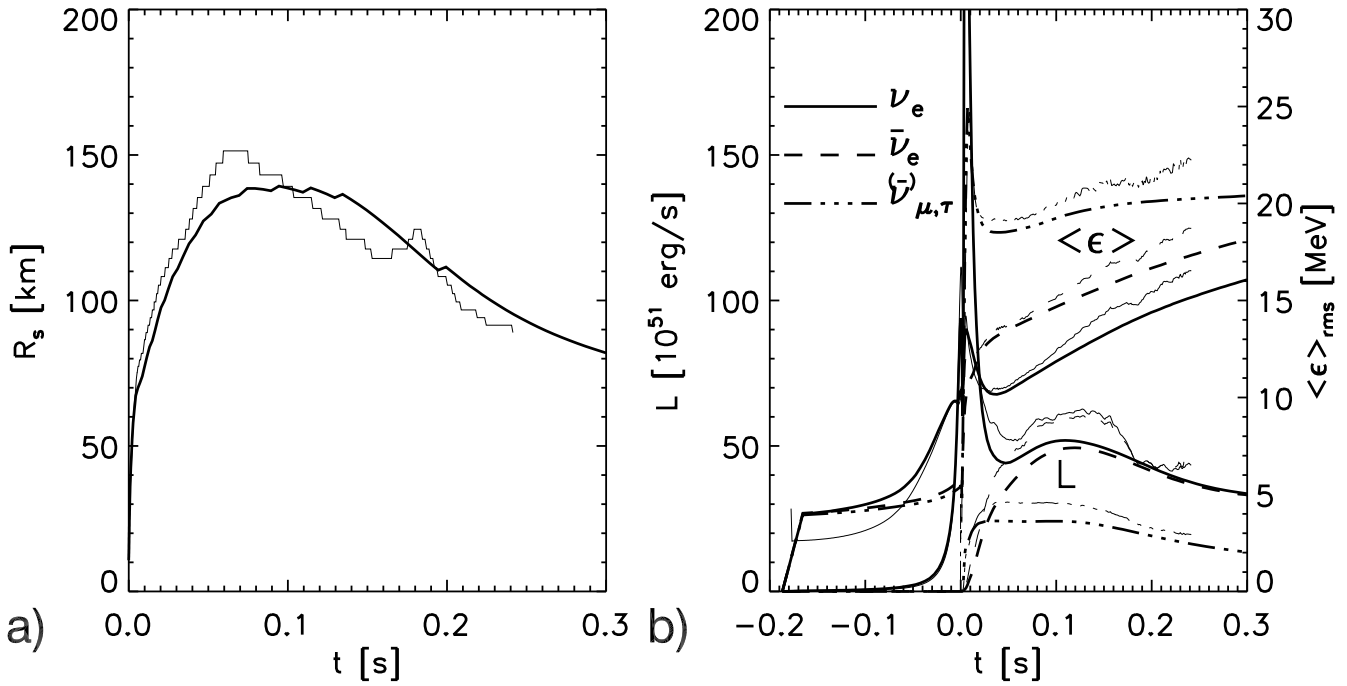

FIG. 9.— The shock position as a function of time for model G15 is displayed in graph (a). The shock in VERTEX (thin line) propagates to a larger maximal radius than in AGILE-BOLTZTRAN (thick line). It retracts to a $\sim$ 10 km smaller radius afterwards. The VERTEX simulation resolves the structure of the outer layers of the progenitor star more accurately than the diffusive adaptive grid in AGILE-BOLTZTRAN. The hump in the VERTEX shock position at $\sim$ 180 ms after bounce corresponds to an entropy and density discontinuity at the bottom of the oxygen-rich silicon shell. The neutrino luminosities and rms energies are presented as functions of time in graph (b). The values are sampled at a radius of 500 km in the comoving frame. The solid lines belong to electron neutrinos, the dashed lines to electron antineutrinos, and the dash-dotted lines to μ- or τ-neutrinos (or their antiparticles). The line width distinguishes between the results from AGILE-BOLTZTRAN and VERTEX in the same way as in graph (a). The differences in the electron flavor neutrino luminosities may in part reflect differences in the increasingly relativistic accretion flow. A part of $2-4\%$ differences in the electron flavor neutrino luminosities and 8% differences in the μ- and τ-neutrino luminosities stem from the inclusion of neutrino-antineutrino production by nucleon-nucleon bremsstrahlung in VERTEX.

still slightly stronger shock in VERTEX) and the density profiles in graph (b) differ mainly behind the shock. In contrast to the N13 case, VERTEX appears to predict at this location a higher density than AGILE-BOLTZTRAN. However, steep density profiles have to be read with care. If we compare the conditions around the shock, the shock position should be taken as reference location and not the center of the star. After shifting the profiles of the models such that the shock positions match in graph (b) we find a higher density in AGILE-BOLTZTRAN close to the shock and a higher density in VERTEX somewhat farther behind the shock. This is perfectly consistent with the entropy profiles in graph (d). Initially the shock is stronger in AGILE-BOLTZTRAN and leaves higher entropy behind. Later the shock in VERTEX is stronger and the relation between the entropies is inverse. This difference is enhanced by a marginally earlier launch of the neutrino burst in AGILE-BOLTZTRAN. The lepton fractions in graph (d) demonstrate that at the considered time more deleptonization has occurred in AGILE-BOLTZTRAN than in VERTEX. These facts explain the higher density behind the shock in the shifted AGILE-BOLTZTRAN profile by the compression compensating for lower electron fraction and entropy.

The time dependent data in Fig. 9, graph (a), show shock trajectories with maximum deviations of order 10%. The VERTEX shock propagates initially farther out. This causes a faster recession after the maximum radius is reached to find to a similar equilibrium as the shock in AGILE-BOLTZTRAN. In VERTEX, the shock transiently re-expands at 150 ms and finds back to an average track that is at slightly smaller radii than the shock trajectory in AGILE-BOLTZTRAN. These features in the VERTEX simulation are caused by the more accurate tracking of layer interfaces outside of the iron core. The transition from the iron to the silicon layer passes the shock around 45 ms after bounce (causing in VERTEX a first bump of the shock trajectory which enhances the shock expansion to a larger maximum radius at about 60 ms post bounce) and the interface to the oxygen-rich silicon layer passes at about 150 ms after bounce. The former is treated in AGILE-BOLTZTRAN as an instantaneous burning front while the latter interface has been neglected in the simulation. The time evolution of the luminosities and rms energies in graph (b) reveals larger values in the VERTEX run. We might be tempted to interpret the larger luminosities as a consequence of the increased accretion rate during the more pronounced shock recession around 100 ms after bounce, but we will make this argument more precise in the discussion of late time slices.

We present two time slices for the longterm evolution of the G15 simulation. The first time slice is at 100 ms after bounce when the neutrino heating is most efficient. The second time slice at 237 ms marks the end of the time range

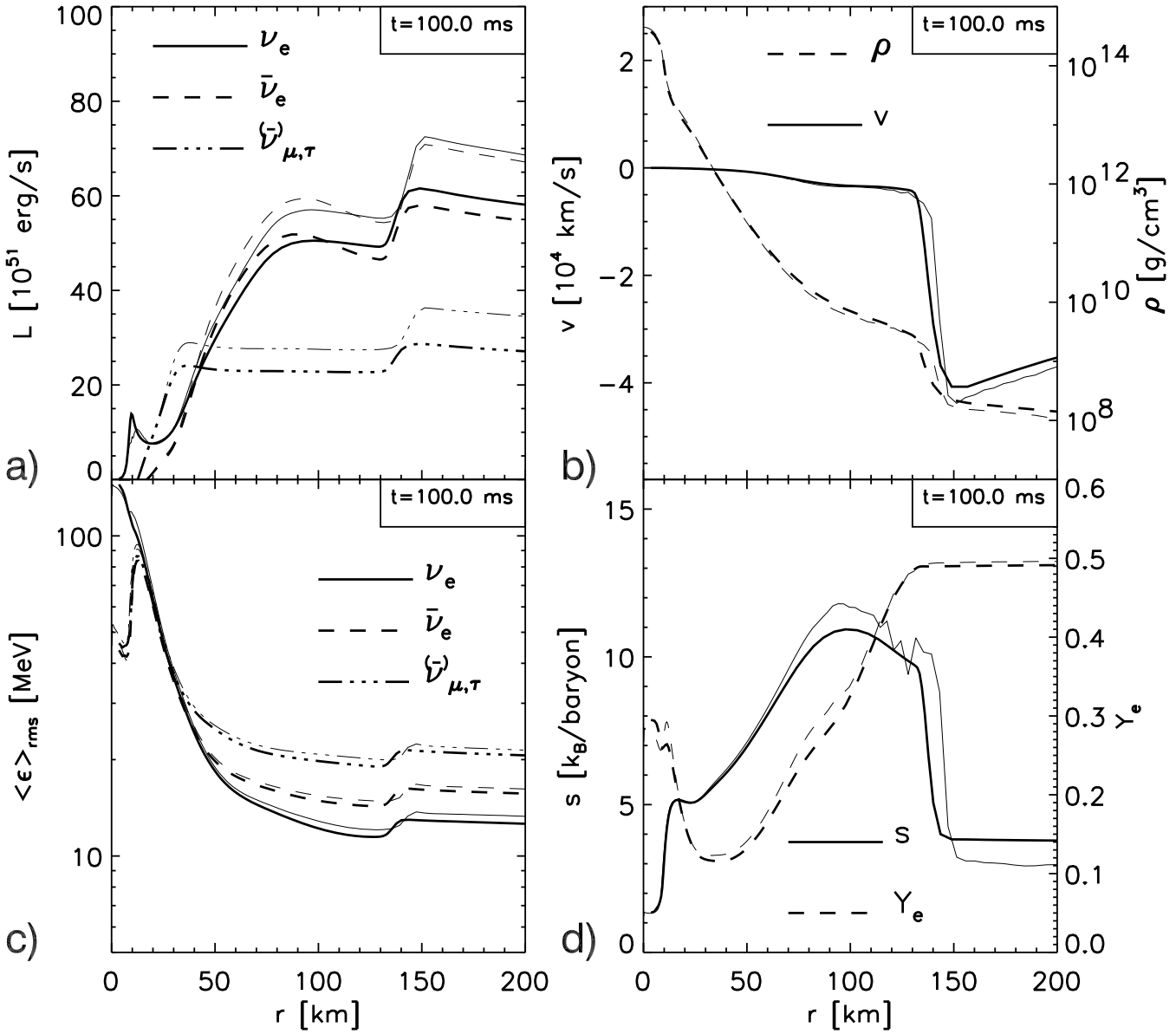

FIG. 10.— Snapshot at 100 ms after bounce for model G15. Data from the AGILE-BOLTZTRAN simulation are drawn with a thick line. Data from the VERTEX simulation are drawn with a thin line. Graph (b) shows the velocity (solid lines) and density (dashed lines) profiles, graph (d) the entropy (solid lines) and electron fraction (dashed line). The neutrino luminosities and rms energies are shown in graphs (a) and (c) respectively. Solid lines refer to electron neutrinos, dashed lines to electron antineutrinos, and dash-dotted lines to μ- or τ-neutrinos (or their antiparticles). In this time slice we find a larger shock position and slightly larger post-shock infall velocities in VERTEX compared to the results of AGILE-BOLTZTRAN. Consistent with the more compact structure of the protoneutron star, the entropies, neutrino luminosities, and neutrino rms energies in VERTEX are somewhat larger than in AGILE-BOLTZTRAN.

covered by both simulations. Let us continue with a discussion of the first time slice shown in Fig. 10. Graph (b) shows the shock in VERTEX at a slightly larger radius than in AGILE-BOLTZTRAN. The luminosities in graph (a) are about 15% larger in VERTEX. One can also nicely see the luminosity jump across the shock front caused by the Doppler frequency shift and angular aberration for an observer in the comoving frame. It is slightly larger in VERTEX because of the larger velocity jump visible in graph (b). Otherwise the relations between the two runs are just inverse from the situation we analyzed in Fig. 5 for the case of the N13 simulation. Now AGILE-BOLTZTRAN has a higher density in the shocked material in graph (b) and the correspondingly lower entropy and electron fraction in graph (d). Also the neutrino rms energies in graph (c) are now lower than in the VERTEX simulation.

This combination of higher luminosities, higher rms energies and higher entropies at the neutrinosphere reminds us of the differences found between Newtonian and general relativistic simulations, where they are due to differences between the Newtonian and relativistic gravitational potential (e.g. (Bruenn, DeNisco, & Mezzacappa 2001)). However, both of our simulations are designed to reproduce an accurate solution to the Tolman-Oppenheimer-Volkoff equation for the hydrostatic structure of the protoneutron star. The differences more likely stem from differences in the enclosed mass that generates the effective gravitational potential. One reason is the lower density of AGILE-BOLTZTRAN in the region between an enclosed mass of 0.5 $M_\odot$ and 1.5 $M_\odot$ in Fig. 7b. Fig. 8b shows that this density deviation outside of the shock at bounce is accreted through the shock after bounce. The difference in the density profiles appears at bounce and might be a consequence of the diffusivity of the first order advection prescription of the adaptive grid in AGILE when high grid velocities occur to resolve the steepening shock front. The enclosed mass accumulated in the protoneutron star of the AGILE-BOLTZTRAN simulation grows more slowly. The deviation in the mass enclosed within 100 km radius is 2% at 50 ms after bounce and stays fairly constant afterwards. Another possible cause are neglected relativistic effects in the kinematics of the VERTEX simulation. When the preshock values of the infall velocities reach several percent of the speed of light, the Newtonian infall velocities might be an overestimate with respect to the relativistic velocities calculated in AGILE-BOLTZTRAN. However, this would only have a transient consequence because the time-integrated mass flux is finally determined by the outer layers which feed the accretion flow from a region where relativistic effects are negligible. We point also to the fact that the early deviation in the accumulated mass has the potential to amplify itself. Once more mass has accumulated, the emptied surroundings draw more additional mass inwards from the outer layers and the effective gravitational potential at a given radius increases. The inclusion of nucleon-nucleon bremsstrahlung in the VERTEX simulation also contributes to the higher compactness of the protoneutron star. This reaction accelerates the energy loss with an 8% increase in the μ- and τ-neutrino luminosities while the electron flavor neutrino luminosities are increased by $2-4\%$ as a consequence of the more rapid neutron star contraction; cf. models B1 and S1 in Fig. 4 in Janka et al. (2002)).

The primary source of the differences in the longterm evolution might be caused by yet another effect, which we indeed consider to be the most likely explanation, namely the different resolution of the structure of the outer layers in our simulations. An infalling high density region in VERTEX (which has been smoothed by "burning" and adaptive grid diffusivity in AGILE-BOLTZTRAN) transiently enhances the accretion rate between 50 ms and 150 ms after bounce. This leads to the reduction in the shock radius in Fig. 9a and to part of the luminosity increase in Fig. 9b. When the transition to the oxygen-rich silicon layer (which has not been considered in the AGILE-BOLTZTRAN simulation) falls in shortly before 200 ms after bounce, the accretion rate decreases sharply and the shock in the VERTEX simulation can transiently expand. This is again consistent with the luminosity reduction at the same time instance.

We also include the latest time slice at 237 ms after bounce in Fig. 11. The graphs show the same qualitative features we have discussed in the context of Fig. 10. The VERTEX data are somewhat noisier because the periodical regridding is overdue at this time.

4.3. *Discussion*

This work extends fine testing of our codes beyond the independently performed calculations of idealized problems with analytical solutions (Messer 2000; Rampp & Janka 2002; Liebendörfer, Rosswog, & Thielemann 2002; Liebendörfer et al. 2004). Here we directly compare the results of the codes in the application they were actually developed for. Our aim was to assess quantitative differences in these highly complex calculations and by that reduce reasons for expecting qualitative differences in future applications. We also intended to create a reference for future code comparisons that is by far more realistic than idealized test cases, but that is also much more accessible than simulations with multidimensional degrees of freedom (e.g. in (Janka et al. 2002)).

We have encountered two fundamental difficulties in our comparison. The first is the fact that the two codes employ different methods, use different basic quantities, and are differently structured. Although it is straightforward to compare the physical quantities the two approaches aim to predict, it is by far more challenging (and sometimes impossible) to track differences back to their origin if the involved quantities are not calculated along the same line. The second difficulty is more related with the supernova physics than with the methodology. There is always a strong feedback between most of the quantities. In the comparison of our results we have very often encountered the situation that the evolution of all quantities is perfectly consistent within both of our implementations, but not exactly the same. Further investigations of the differences revealed small initial differences in all coupled quantities that grow with ongoing evolution time. Only in rare cases it was possible to separate cause and consequences. On the other hand, this strong coupling between quantities also indicates that the problem is governed by many equilibria. As soon as equilibrium is achieved the codes converge again and find back to a similar evolution. This is for example the case in N13 when stationary-state accretion is established.

If we consider just the overall dynamical evolution of the spherically symmetric postbounce phases in Figs. 4 and 9, we find agreement in all qualitative features of the history. But we also find some significant quantitative differences. For example, the early shock propagation or the luminosities during the first 100 ms after bounce are different in model N13. We attribute an important part of these differences to the hydrodynamic shock propagation that appears to maintain a stronger shock in VERTEX than in AGILE-BOLTZTRAN. The close coincidence of the neutrino burst with the transition from a dynamic to an accretion shock in this model leads to a dramatic amplification of the existing difference. The region behind the shock in AGILE-BOLTZTRAN deleptonizes to a larger extent by a neutrino burst of longer duration than in VERTEX. Hence, the VERTEX core may maintain higher luminosities for a longer time. This may be the cause for a somewhat more optimistic shock propagation in the early phase of the VERTEX simulation of

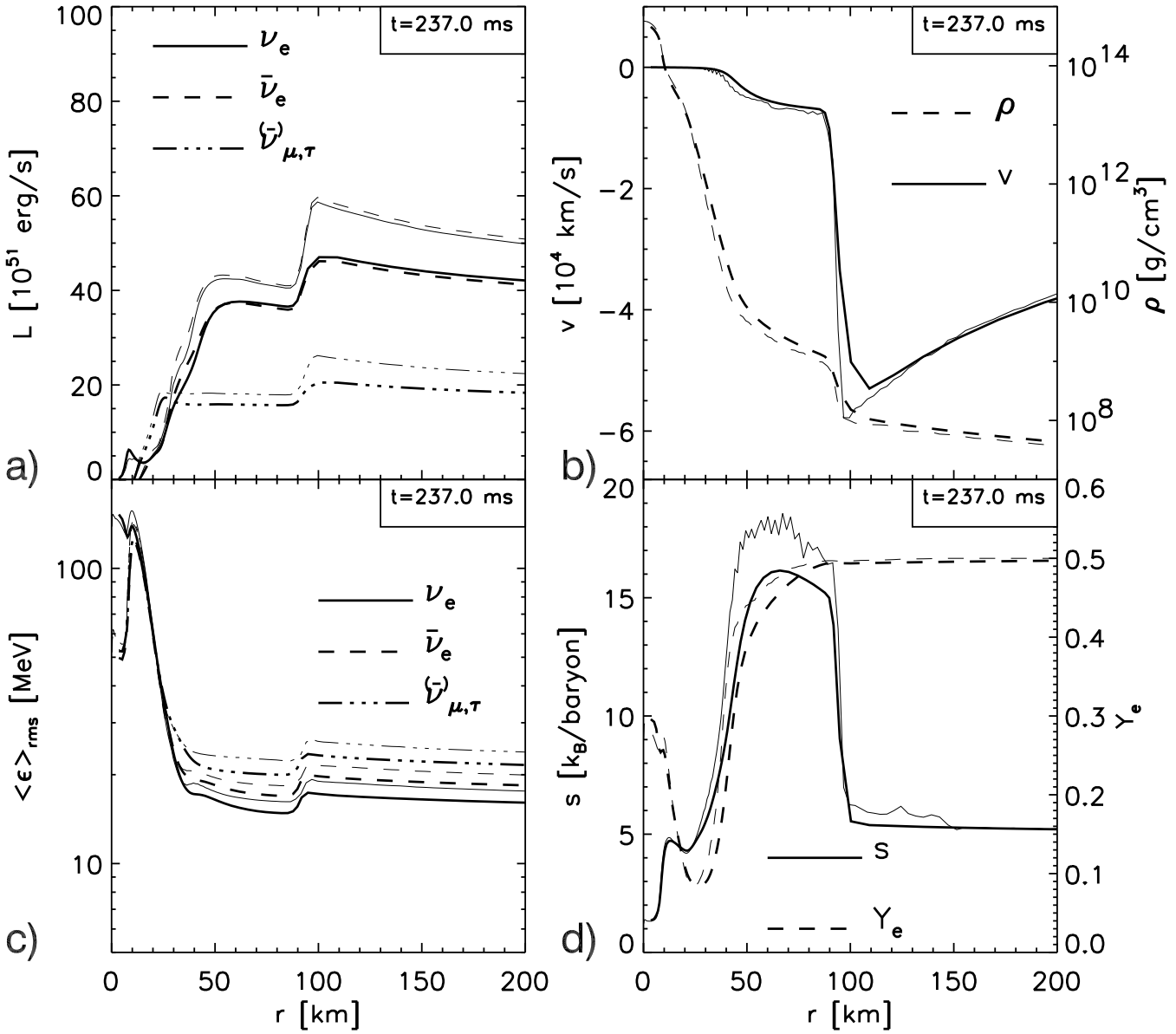

FIG. 11.— Snapshot at 237 ms after bounce for model G15. Data from the AGILE-BOLTZTRAN simulation are drawn with a thick line. Data from the VERTEX simulation are drawn with a thin line. Graph (b) shows the velocity (solid lines) and density (dashed lines) profiles, graph (d) the entropy and lepton abundances. The neutrino luminosities and rms energies are shown in graphs (a) and (c). Solid lines refer to electron neutrinos, dashed lines to electron antineutrinos, and dash-dotted lines to μ- or τ-neutrinos (or their antiparticles). The quantitative differences between AGILE-BOLTZTRAN and VERTEX are similar to those found in Fig. 10 at 100 ms after bounce.

the evolution of model N13.

This amplification effect of the neutrino burst is absent in the G15 model where the shocks in both runs have reached the accretion mode when they plough through densities which allow neutrinos to escape quickly. These two more realistic runs with "standard" input physics as implemented by each group agree nicely and differences appear only in a later phase, when the differently handled outer layers of the progenitor fall into the shock front. We find good agreement in the diffusive inner core of the protoneutron star. We find excellent agreement in the timing and peak height of the neutrino burst. The approximations of the general relativistic effects in VERTEX do not seem to introduce any larger differences to the general relativistic approach than other acceptable uncertainties. This outcome is especially useful for multi-dimensional simulations, where the important general relativistic effects

should not be neglected, but where a general relativistic ansatz might not have immediate priority. In the general relativistic G15 simulations, we found differences due to different input physics, adaptive grid effects, and different treatment of the outer layers. Since the representation of the general relativistic potential in VERTEX was designed to accurately describe hydrostatic configurations (Rampp & Janka 2002) it is unlikely that there are large differences in the effective gravitational potential. However, the mass infall rate and thus the growth rate of the protoneutron star might be overestimated by the disregard of relativistic kinematics in the Newtonian hydrodynamics code employing a modified gravitational potential. It was neither possible to confirm nor to dispel such differences among the other differences. This underlines their modest relevance in spherically symmetric simulations up to 240 ms after bounce.

Both methods have their vulnerabilities and some of them have led to lively discussions in the past. AGILE-BOLTZTRAN has been criticized because of the rigorous approach and the generous consumption of computer memory and cpu time. The resolution of the neutrino phase space is considered to be at the lower justifiable limit in these simulations. And indeed, the certainty that the evolution follows basic physical principles independently of the resolution must be earned by very specific twists and wrinkles in the finite difference representation. VERTEX has raised concerns with regard to consistency as it uses disjunct gridding for radiation transport and hydrodynamics and applies a regridding procedure after bounce. And the fact that the transport equations for neutrino number and neutrino energy are solved separately does not reduce complexity. However, we did not find discrepancies in our comparison that would support any of these concerns to a degree that would question the reliability of the qualitative results in our explosion-free supernova simulations.

The different strengths of the codes are more visible in the quantitative details of the calculations. VERTEX produces great angular resolution in the flux factors even far from the neutrinospheres and keeps properly track of the sharp discontinuities in the composition of the outer layers. Its extendibility to two-dimensional simulations is built-in (Rampp & Janka 2002) and the general relativistic approximation can be expected to produce accurate results in multi-dimensional situations as well (Buras et al. 2003). However, the solution of a model Boltzmann equation is much more involved in more than one dimension. Additional approximations introduced by spherical averaging or ray-by-ray techniques cannot be tested in a comparison between spherically symmetric models. If these approximations are good, the variable Eddington factor approach is a very efficient technique for multidimensional simulations.

AGILE-BOLTZTRAN demonstrates that the solution of only one transport equation for the neutrino distribution function can provide accurate radiation transport solutions in the diffusion limit and semi-transparent regime. Number and energy conservation properties are reasonably met and the description of hydrodynamics and radiation transport add up to one consistent general relativistic finite difference representation of radiation hydrodynamics in spherical symmetry (Liebendörfer et al. 2004). The approach is in principle extendible to two and three dimensions and allows for adaptive zoning because it is based on the local description of the transport equation in confined fluid elements. But consistency is easily lost in multiple dimensions (Cardall & Mezzacappa 2003) and computer performance may become prohibitive in an implicit multidimensional discrete ordinates approach.

5. CONCLUSIONS

We have compared two different approaches to implement Boltzmann neutrino transport in spherically symmetric radiation hydrodynamics simulations of stellar core collapse and postbounce evolution. We performed calculations for two different progenitor stars, the 13 $M_\odot$ progenitor of Nomoto & Hashimoto (1988) and the 15 $M_\odot$ progenitor of Woosley & Weaver (1995). We intended to present one calculation with matched minimum input physics that leads to a plausible scenario after bounce and a second calculation with the "standard" physics as handled by each group. We expected therefore very good agreement in the first case and less perfect agreement in the second case because of possible differences in the input physics. The result was almost inverse: An interesting coincidence of the launch of the neutrino burst with the transition of the hydrodynamic shock from the dynamic to the accretion phase was triggered differently in the two N13 simulations, such that initial differences from the hydrodynamic shock propagation were dramatically amplified. We found that a neutrino burst from an accretion shock is maintained for a longer time than a neutrino burst from a dynamic shock. Infalling matter is squeezed more efficiently in an accretion shock and more electron captures on free protons are maintained in the denser matter after the transition of the shock. After this initial phase of dynamical differences, the N13 runs converge again and find back to excellent agreement in the maximum shock expansion and the following quasi-stationary accretion phase. Qualitatively similar differences can be seen in the G15 run. However, the shock forms at a smaller enclosed mass in this general relativistic model and additional energy is lost by the inclusion of μ- and τ-neutrinos. The neutrino burst is then launched from an accretion shock in both models and initial differences are not amplified as in the Newtonian calculation where we found a significantly stronger bounce-shock.

Thus, the general evolution in both models is in agreement. Differences in details are found, e.g. a stronger hydrodynamic shock in PROMETHEUS and more artificial diffusion in the composition of progenitor layers in AGILE. The luminosities in VERTEX tend to be slightly larger than in AGILE-BOLTZTRAN and the rms energies a little lower. The approximated general relativistic effects by using a modified gravitational potential in a Newtonian hydrodynamics code may produce a marginally deeper potential due to faster mass infall. Larger differences stem rather from implementation- than method-specific details, e.g. the use of the low-order advection scheme in AGILE-BOLTZTRAN or specific selections of the finite differencing in both codes.

We come to the conclusion that both methods work satisfactorily in this application and give comparable results. We determined similar computational needs for our not thoroughly optimized codes. Standard runs with AGILE-BOLTZTRAN appear to be tendentially faster. But standard runs in VERTEX have been performed with better energy

resolution and the applied angular resolution in outer regions is unachievable by S_N methods. Hence, an accurate comparison of cpu requirements is impossible and meaningless. Moreover, faster methods may have been developed in the mean time (Burrows et al. 2000; Thompson, Burrows, & Pinto 2003). Rather than arguing for the "best" method for a certain application, we recommend to pursue a variety of feasible numerical approaches for future astrophysical simulations in the interest of independent mutual validation of the results. We hope that our comparison provides a step towards quantitative astrophysics in a very complex environment.

ACKNOWLEDGMENTS

We thank R. Buras and O. E. B. Messer for many important contributions to VERTEX and AGILE-BOLTZTRAN respectively, in particular for implementing the three-flavor versions of the codes and coining subroutines to calculate the neutrino pair and bremsstrahlung rates. We are greatly indebted to Chris Fryer for suggesting and promoting this comparison. The Institute for Nuclear Theory at the University of Washington is acknowledged for its hospitality and the Department of Energy for support during a visit of the Summer Program on Neutron Stars in 2001, during which we started this work. AM and ML acknowledge funding by the NSF under contract AST-9877130, the Oak Ridge National Laboratory, managed by UT-Batelle, LLC, for the U.S. Department of Energy under contract DE-AC05-00OR22725, and the DoE HENP SciDAC Program. HTJ and MR are grateful for support by the Sonderforschungsbereich 375 on "Astroparticle Physics" of the Deutsche Forschungsgemeinschaft. The computations of the Garching group were mostly performed on the CRAY T90 and CRAY SV1ex of the John von Neumann Institute for Computing (NIC) in Jülich and the computations of the Oak Ridge-Basel group on the NERSC CRAY SV-1.

REFERENCES

Bethe, H. A. & Wilson, J. R. 1985, ApJ, 295, 14
Bludman, S. A. & Cernohorsky, J. 1995, Phys. Rep., 256, 37
Bruenn, S. W. 1985, ApJS, 58, 771
Bruenn, S. W. & Mezzacappa, A. 1997, Phys. Rev. D, 56, 7529
Bruenn, S. W., DeNisco, K. R., & Mezzacappa, A. 2001, ApJ, 560, 326
Buras, R., Rampp, M., Janka, H.-Th., & Kifonidis, K. 2003, Phys. Rev. Lett., 90, 241101
Burrows, A., Young, T., Pinto, P., Eastman, R., & Thompson, T. A. 2000, ApJ, 539, 865
Calder, A. C., Fryxell, B., Plewa, T., Rosner, R., Dursi, L. J., Weirs, V. G., Dupont, T., Robey, H. F., Kane, J. O., Remington, B. A., Drake, R. P., Dimonte, G., Zingale, M., Timmes, F. X., Olson, K., Ricker, P., MacNeice, P., Tufo, H. M. 2002, ApJS, 143, 201
Cardall,C. Y., Mezzacappa, A. 2003, Phys. Rev. D, 68, 023006
Cernohorsky, J. 1994, ApJ, 433, 247
Colella, P. & Woodward, P. 1984, J. Comp. Phys., 54, 174
Dorfi, E. A., & Drury, L. O'C. 1987, J. Comput. Phys., 69, 175
Einfeldt, B. 1988, SIAM Jour. Numer. Anal., 25, 294
Fryxell, B., Müller, E., & Arnett, W. 1989, Hydrodynamics and Nuclear Burning, preprint MPA-449, Max Planck Institut für Astrophysik, Garching
Horowitz, C. 1997, Phys. Rev. D, 55, 4577
Janka, H.-T., Buras, R., Kifonidis, K., Rampp, M., & Plewa, T. 2002, in Review for "Core Collapse of Massive Stars", Ed. C.L. Fryer, Kluwer, Dordrecht, preprint astro-ph/0212314
Keil, W. 1997, PhD thesis, Technische Universität München
Kifonidis, K. 2000, PhD thesis, Technische Universität München
Lattimer, J. & Swesty, F. D. 1991, Nucl. Phys., A535, 331
Liebendörfer, M. 2000, Ph.D. thesis (Basel: University of Basel)
Liebendörfer, M., Mezzacappa, A., & Thielemann, F.-K. 2001, Phys. Rev., D63, 104003
Liebendörfer, M., Mezzacappa, A., Thielemann, F.-K., Messer, O. E. B., Hix, W. R., & Bruenn, S. W. 2001, Phys. Rev., D63, 103004
Liebendörfer, M., Rosswog, S. K., & Thielemann, F.-K. 2002, 141, 229
Liebendörfer, M., Messer, O. E. B., Mezzacappa, A., Bruenn, S. W., Cardall, C. Y., & Thielemann, F.-K. 2004, ApJS preprint doi:10.1086/380191, astro-ph/0207036
Lindquist, R. W. 1966, Ann. Phys., 37, 487
May, M. M., & White, R. H. 1966, Phys. Rev., 141, 1232
Messer, O. E. B. 2000, Ph.D. thesis (Knoxville: University of Tennessee)
Messer, O. E. B., Liebendörfer, M., Hix, W. R., Mezzacappa, A., & Bruenn, S. W. 2003, in Proceedings of the ESO/MPA/MPE Workshop, ed. by Hillebrandt, W. & Leibundgut, B. (Heidelberg: Springer), 70
Mezzacappa, A. & Bruenn, S. W. 1993, ApJ 405, 669
Mezzacappa, A. & Bruenn, S. W. 1993, ApJ 405, 637
Mezzacappa, A. & Bruenn, S. W. 1993, ApJ 410, 740
Mezzacappa, A., Liebendörfer, M., Messer, O. E. B., Hix, W. R., Thielemann, F.-K., & Bruenn, S. W. 2001, PRL, 86, 1935
Mezzacappa, A. & Messer, O. E. B. 1999, JCAM, 109, 281
Misner, C. W., & Sharp, D. H. 1964, Phys. Rev., B136, 571
Myra, E. S., Bludman, S. A., Hoffman, Y., Lichtenstadt, I., Sack, N., & Van Riper, K. A. 1987, ApJ, 318, 744
Nomoto, K. & Hashimoto, M. 1988, Phys. Rep., 163, 13
Plewa, T. & Müller, E. 1999, A&A, 342, 179
Plewa, T. & Müller, E. 2001, Computer Physics Communications, 138, 101
Quirk, J. J. 1994, Int. J. Num. Meth. Fluids, 18, 555
Rampp, M. 2000, PhD thesis, Technische Universität München
Rampp, M. & Janka, H. T. 2000, ApJL, 539, L33
Rampp, M. & Janka, H. T. 2002, A&A, 396, 361
Smit, J. M., Cernohorsky, J., & Dullemond, C. P. 1997, A&A, 325, 203
Sumiyoshi, K., Suzuki, H., Otsuki, K., Terasawa, M., & Yamada, S. 2000, Publ. Astron. Soc. Jap., 52, 601
Takahashi, K., Witti, J., & Janka, H.-T. 1994, A&A, 286, 857
Thompson, T. A., Burrows, A., & Meyer, B. S. 2001, ApJ, 562, 887
Thompson, T. A., Burrows, A., & Pinto, P. A. 2003, ApJ, 592, 434
Tscharnuter, W. M., & Winkler, K. H. 1979, Comput. Phys. Comm., 18, 171
Wanajo, S., Kajino, T., Mathews, G. J., & Otsuki, K. 2001, ApJ, 554, 578
Wilson, J. R. 1985, in Numerical Astrophysics, ed. by Centrella, J. M., LeBlanc, J. M., & Bowers, R. L. (Boston: Jones and Bartlett)
Winkler, K.-H., Norman, M. L., & Mihalas, D. 1984, J. Quant. Spectrosc. Radiat. Transf., 31, 473
Woosley, S. E., Wilson, J. R., Mathews, G. J., Hoffman, R. D., & Meyer, B. S. 1994, ApJ, 433, 229
Woosley, S. E., Weaver, T. A. 1995, ApJS, 101, 181